Tackling the Nature of a White Dwarf Progenitor through Prompt Follow-up Observations of Novae: A Case for V1405 Cas (= Nova Cassiopeiae 2021) as a Low-mass ONeMg White Dwarf

Kenta Taguchi

December 15, 2023

Abstract

A nova is a transient event originated in a binary system consisting of a white dwarf and a late-type companion star. As the hydrogen-rich material accretes onto the white dwarf, explosive nuclear reactions are ignited at the surface of the white dwarf. Thereby the nova launches ejecta, which are likely a mixture of the accreted matter from the secondary as well as the material that has been a part of the white dwarf, either burnt and/or unburnt during the nova explosion. Novae play important roles in binary evolution and cosmic chemical evolution.

Although the initial stage of novae is especially important to study these roles as mentioned above, observing novae in detail during the initial stages has long been difficult until very recently, due to the short duration of the initial brightening stage of novae. This is the main theme of the thesis; we have started a program to take spectra of nova candidates as soon as they are discovered, by making the best use of the recent development in transient surveys. As one of the highlights in this program, we were able to take spectra of the nova V1405 Cassiopeiae, including one taken during its initial rapidly-brightening stage.

We find that V1405 Cassiopeiae showed highly-ionized emission lines of He II and N III only during the initial brightening stage, which confirms the standard theory of the nova dynamics in which the initial rising of a nova is attributed to the temperature decrease caused by the rapid expansion of ejecta. Absorption components of Balmer and helium lines showed decelerating trends in their velocities, which is also naturally explained by the theory.

To quantify the nature of V1405 Cassiopeiae, we have created a framework for relating the density, temperature, and chemical abundance to the emission line strengths, under the one-zone approximation. The modeling not only confirmed the cooling trend as mentioned above, but also reveled peculiar abundances; V1405 Cassiopeiae is rich in nitrogen and aluminum, suggesting that the white dwarf behind V1405 Cassiopeiae is an oxygen-neon-magnesium white dwarf. On the other hand, V1405 Cassiopeiae is a very slow nova, indicating a low-mass nature of the white dwarf, which is usually associated with a carbon-oxygen white dwarf. Our findings suggest the presence of 'very slow neon novae', raising a challenge to the frequently-adopted classification that neon novae always belong to the fast-nova class. Further, it indicates the existence of 'sub-solar-mass oxygen-neon-magnesium white dwarfs', which con-

tradicts the basic single-star evolution models where an oxygen-neon-magnesium white dwarf is predicted to be more massive than a solar mass. Our work thus suggests that a new channel of binary evolution must be involved, e.g., decreasing the mass of oxygen-neon-magnesium white dwarfs after their formation.

Contents

List of Figures

List of Tables

Chapter 1

General Introduction

The **classical nova** is an explosive outburst on the surface of an accreting **white dwarf** (WD, §1.1) caused by the **thermonuclear runaway** (TNR, §1.3), when the mass of the accumulated hydrogen-rich envelope has reached a critical mass (§1.2, Starrfield et al., 1972). The rapid **initial brightening** (by 5–13 magnitudes) in optical wavelengths typically takes place in less than three days. It is then followed by the pre-maximum halt and the final rise of about two magnitudes to the optical maximum, which takes another $\sim$ 1–2 days for fast novae or several weeks for the slowest novae (see Figure 2.2 of Bode & Evans 2008 and Strope et al. 2010 for the optical light curves of novae). Here, the '**speed class**', i.e., whether a nova is fast or slow, is conventionally defined by the decay speed in the decline phase after the maximum light[1], and theoretically considered to relate to the mass of the WD ($M_{\rm WD}$, §1.5). Since novae are by thermonuclear reactions on the surface of WDs, due to the uniqueness of the environment, it is considered to be the origins of some kinds of nuclei (§1.4). In the rest of this chapter, I briefly review important properties of novae for this thesis mostly on theoretical aspects.

1.1 Single Star Evolution and White Dwarfs

White dwarfs (WDs), stellar core remnants supported by the degenerate pressure of electrons, are the common end of stellar evolution for low-mass stars. As the hydrogen burning at the center of a main sequence star progresses, a helium core is formed in the center, and finally, hydrogen is depleted in the core. Then, the helium core cannot help contracting, because it is no longer supported by the hydrogen burning. If the zero-age-main-sequence mass ($M_{\rm ZAMS}$) of the star is greater than $\sim 0.5\ M_\odot$ (Kippenhahn et al., 2013), the helium core contraction leads to helium burning to support the star again. If the mass is smaller, on the other hand, the electron degeneracy will be able to support the helium core before the helium core contracts denser enough to start helium burning (Prialnik, 2009, see also Figure 1.1).

[1] In this thesis, we follow Payne-Gaposchkin (1964) to determine the speed class. For Galactic novae before 2010, we use decline times given by Strope et al. (2010).

In this case, the star ejects its envelope to remain a helium white dwarf (He WD[2]). In the same way, a **carbon-oxygen white dwarf** (CO WD) remains if $M_{\rm ZAMS}$ is between $\sim 0.5\ M_\odot$ and $\sim 8\ M_\odot$, and an **oxygen-neon-magnesium white dwarf** (ONeMg WD) remains[3] if $M_{\rm ZAMS}$ is between $\sim 8\ M_\odot$ and $\sim 10\ M_\odot$. If $M_{\rm ZAMS}$ is larger than that, the star continues nuclear burning until it forms an iron core to hold a type-II supernova (SN II, Maeda, 2022).

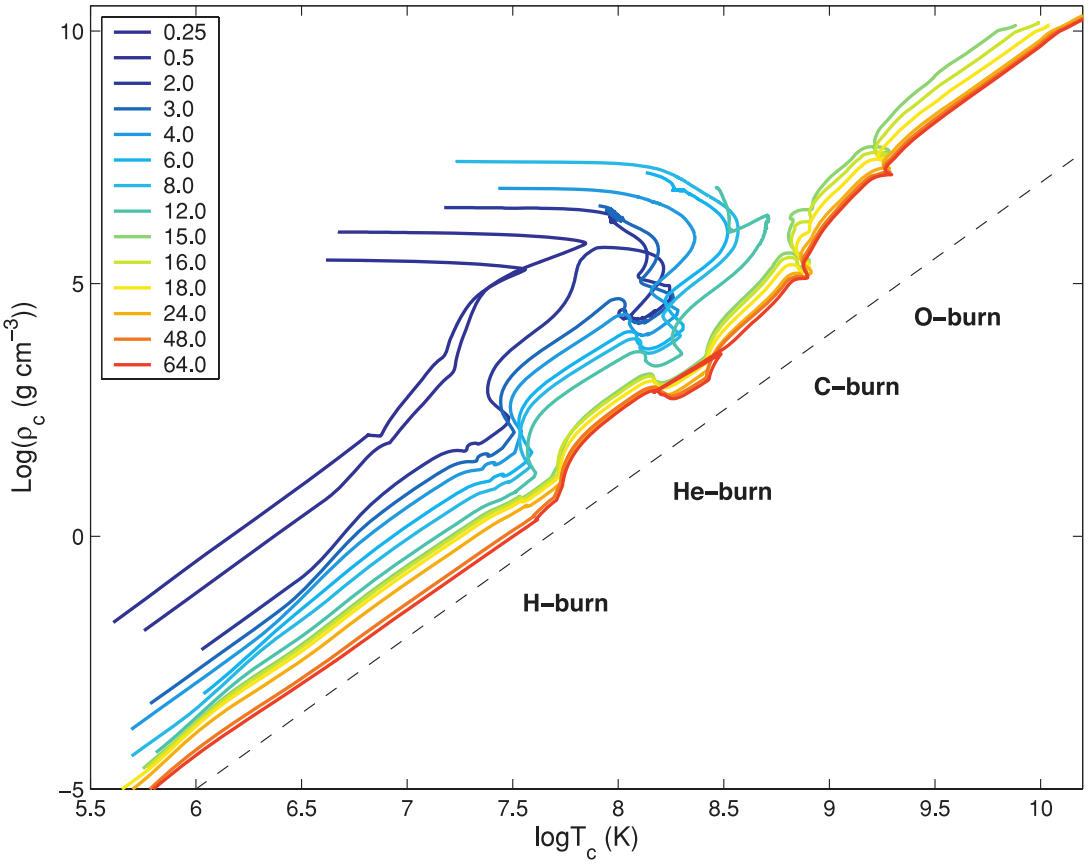

Figure 1.1: Evolution of the central temperature ($T_{\rm c}$) and density ($\rho_{\rm c}$) for population I ($Z = 0.018$) stellar models having different initial masses ($0.25 - 64\ M_\odot$). $\rho_{\rm c}$ in a lower-mass model asymptotes to a value, at which the whole core can be supported by the degenerate pressure to evolve the star a WD. Adopted from Figure 9 in Kovetz et al. (2009), "A new, efficient stellar evolution code for calculating complete evolutionary tracks".

1.2 Novae and Recurrent Novae

A nova occurs in a close binary consisting of a WD and a late star (e.g., cataclysmic variables) or in a binary consisting of a WD and a red giant (e.g., symbiotic stars). In those binary systems, hydrogen-rich

[2]Such a low-mass stars have longer main-sequence lifetimes than the age of the Universe (Mowlavi et al., 2012).
[3]More precisely, stars within a nallow range of this interval are thought to have an electron-capture supernova (ECSN, Nomoto, 1984; Miyaji et al., 1980; Langer, 2012) and not to remain an ONeMg WD.

material accretes onto the surface of the white dwarf. Once the mass of the accreted matter accumulated on the surface of the WD reaches a critical limit, the explosive hydrogen burning onsets (thermonuclear runaway, TNR, see also §1.3), leading to the brightening and the mass ejection[4]. Once the hydrogen is ejected/spent out, the WD returns to the quiescent, accreting phase; the WD will experience the next nova again in the future after enough mass has accreted. The interval between one nova eruption and the next is, for most systems, much longer than 100 years. The interval between one nova eruption and the next is, for most systems, much longer than 100 years. However, for about ten systems like U Sco (Starrfield et al., 1988; Hachisu et al., 2000), T CrB (Schaefer, 2023), RS Oph (Hachisu & Kato, 2001; O'Brien et al., 2006; H. E. S. S. Collaboration et al., 2022), V3890 Sgr (Page et al., 2020), T Pyx (Shore et al., 2011; Ginzburg & Quataert, 2021), or M31 N2008-12a (White et al., 1995; Tang et al., 2013; Kato et al., 2014), their intervals are short enough that two or more past nova eruptions have been recorded for those systems ('recurrent novae' or 'RNe'). For most RNe, their intervals are fairly periodic; therefore known RNe are monitored by many observers including amateur astronomers, and there are some attempts to find past outbursts of RNe. For example, Schaefer (2023) reports the past activity of T CrB from ancient documents. For the recurrent nova M31N 2017-01e recently confirmed (Shafter et al., 2022); for this object I contributed by surveying the past records to discover the 2012 outburst, named M31N 2012-01c, from the Pan-STARRS data (and by giving some ideas on the discussion).

Theoretically, the interval is considered short if the mass of the WD ($M_{\rm WD}$) and/or the mass-accretion rate ($\dot{M}$) is high. Hereafter, standard astrophysical terms/symbols are used without introduction. As a simple estimation, assuming that the gravitational energy release of the accreted matter on the WD and the radiation cooling from the WD balance,

$$\frac{GM_{\rm WD}\dot{M}}{R_{\rm WD}} \sim 4\pi R_{\rm WD}^2 \sigma_{\rm SB} T_{\rm env}^4. \tag{1}$$

Here, $R_{\rm WD}$ and $T_{\rm env}$ are the radius and temperature of the WD surface (= the H-rich envelope), and $\sigma_{\rm SB}$ is the Stefan-Boltzmann constant. Also, considering the hydrostatic balance in the accreted layer,

$$\frac{{\rm d}P}{{\rm d}r} = -\frac{GM_{\rm WD}\rho}{4\pi r^2}, \tag{2}$$

and the equation of continuity,

$$\frac{{\rm d}m}{{\rm d}r} = 4\pi r^2 \rho, \tag{3}$$

[4]However, if the mass accretion rate is high enough, persistent nuclear burning on the surface of the WD becomes possible. In this case, the WD will be observed as a super-soft X-ray source or a 'born-again giant' rather than a transient nova (Ginzburg & Quataert, 2021).

the pressure at the bottom of the H-rich envelope is estimated as,

$$P_{\rm env} \sim \frac{GM_{\rm WD}M_{\rm env}}{R_{\rm WD}^4}. \tag{4}$$

Here, $M_{\rm env}$ is the mass of the H-rich envelope. From (1) and (4), if the $M_{\rm WD}$[5] and/or $\dot{M}$ are large, $T_{\rm env}$ and/or $P_{\rm env}$ are high, and therefore the H-rich envelope is easy to start H-burning (so $M_{\rm env}$ required to start H-burning and the recurrent time is also small).

1.3 The Secular (Thermal) Instability/Stability

In this section, we consider the stability/instability of stellar systems producing energy by burning fuel. The basic equations are

$$\frac{{\rm d}P}{{\rm d}r} = -\frac{Gm\rho}{r^2} \qquad \text{(pressure balance)}, \tag{5}$$

$$\frac{{\rm d}m}{{\rm d}r} = 4\pi r^2\rho \qquad \text{(equation of continuity)}, \tag{6}$$

$$\frac{{\rm d}P}{P} = a\frac{{\rm d}\rho}{\rho} + b\frac{{\rm d}T}{T} \qquad \text{(equation of state)}. \tag{7}$$

For ideal gas, $a = b = 1$, and for non-relativistic degenerated gas, $a = \frac{5}{3}$ and $b = 0$.

Assuming that there is a perturbational excess/loss of energy ${\rm d}q$ from the static structure. From the first law of thermodynamics, the effect of energy excess is estimated as

$${\rm d}q = c_{\rm P}T\left(\frac{{\rm d}T}{T} - \nabla_{\rm ad}\frac{{\rm d}P}{P}\right). \tag{8}$$

Here,

$$\nabla_{\rm ad} \equiv \left(\frac{\partial \ln T}{\partial \ln P}\right)_s = \frac{bP}{aT\rho c_P}. \tag{9}$$

If another relation between the derivatives is specified (e.g., (10) or (20)) in addition to (8) and the equation of state (7), the equations are closed and one can find if ${\rm d}q$ and ${\rm d}T$ have the same signs (secular instability) or not (secular stability[6], the 'negative gravothermal specific heat').

As an example, for the ideal gas ($a = b = 1$) case with the polytropic relation,

$$P = K\rho^{1+1/n}, \tag{10}$$

[5] Note that, for white dwarfs, $R_{\rm WD}$ is small if $M_{\rm WD}$ is large.

[6] Strictly speaking, whether the temperature runs away or not also depends on the dependency of energy production/transfer upon T (e.g., see §25.3.5 of Kippenhahn et al., 2013).

holds[7],

$$\frac{\mathrm{d}q}{c_P T} = \frac{3-2n}{5n}\frac{\mathrm{d}\rho}{\rho} = \frac{3-2n}{5(n+1)}\frac{\mathrm{d}p}{p} = \frac{3-2n}{5}\frac{\mathrm{d}T}{T}. \tag{11}$$

By dimensional analysis (see e.g., Prialnik, 2009), the central pressure P_c and density ρ_c are related as

$$P_\mathrm{c} = (4\pi)^{1/3} B_n G M^{2/3} \rho_\mathrm{c}^{4/3}. \tag{12}$$

and therefore $n = 3$ holds and the system is stable (here B_n is the proportionality coefficient depending on n). On the other hand, for the non-relativistic degenerated gas ($a = \frac{5}{3}$, $b \to +0$),

$$\frac{\mathrm{d}q}{c_P T} = \frac{\mathrm{d}T}{T} \tag{13}$$

and therefore the system is unstable.

In the case of novae, $\mathrm{d}q$ (> 0) occurs within a thin shell on the surface of the WD[8]. Consider a thin shell, whose mass coordinates at the inner and outer boundaries are $m - \Delta m$ and m, is in a static balance. From (5) and (6), the pressure at m is

$$P(m) = \int_m^M \frac{Gm'}{4\pi(r(m'))^4}\,\mathrm{d}m' \tag{14}$$

Assuming that, as a responce to an energy excess $\mathrm{d}q$ (> 0) within the shell, the material outside $r(m)$ expands homologously (i.e., $\frac{\mathrm{d}r(m)}{r(m)}$ does not depends on m),

$$\mathrm{d}P(m) = \int_m^M \left[\frac{Gm'}{4\pi(r(m') + \mathrm{d}r(m'))^4} - \frac{Gm'}{4\pi(r(m'))^4}\right]\mathrm{d}m' \tag{15}$$

$$\approx -4\int_m^M \frac{Gm'}{4\pi(r(m'))^4}\frac{\mathrm{d}r(m')}{r(m')}\,\mathrm{d}m' \tag{16}$$

$$= -\frac{4\mathrm{d}r(m)}{r(m)}\int_m^M \frac{Gm'}{4\pi(r(m'))^4}\,\mathrm{d}m', \tag{17}$$

and therefore

$$\frac{\mathrm{d}P}{P} = -4\frac{\mathrm{d}r}{r}. \tag{18}$$

Also assuming the inner boundary of the shell $r(m - \Delta m)$ unchanged,

$$\frac{\mathrm{d}\rho}{\rho} = -\frac{\mathrm{d}(\Delta r)}{\Delta r} = -\frac{\mathrm{d}r(m)}{\Delta r}. \tag{19}$$

Here, we have used $4\pi(r(m-\Delta m))^2\,\mathrm{d}(\rho\,\Delta r) = \Delta m = 0$, with denoting the thickness of the shell

[7] This relation does not have to (or should not) be interpreted as an equation of state; it just gives (specifies) another relationship between P and rho independent from the EoS (by considering an adiabatic process, for example). This relation degenerates with the EoS in the specific case where we don't have to solve T (T does not appear on the EoS).

[8] The situation is similar to the 'pulse instability' in asymptotic giant branch stars (e.g., Schwarzschild & Härm, 1965). See also §34.2 of Kippenhahn et al. (2013).

$\Delta r \equiv r(m) - r(m - \Delta m)$. Eliminating $\mathrm{d}r$ from above two equations,

$$\frac{\mathrm{d}P}{P} = -\frac{4\Delta r}{r}\frac{\mathrm{d}\rho}{\rho}. \tag{20}$$

Again from the first law of thermodynamics (8) and the equation of state (7),

$$\mathrm{d}q = \left[c_{\mathrm{P}} - \frac{b}{a\rho T\left(1 - \frac{ar}{4\Delta r}\right)}\right]\mathrm{d}T. \tag{21}$$

Considering $\Delta r \ll r$ and therefore the second term is negligible, the shell is unstable. In other words, the perturbation $\mathrm{d}q$ cannot be escaped by the $P\,\mathrm{d}V$ work, and therefore it cannot help being stored as internal energy.

1.4 Daughter Nuclei of Nova

In this section, we review nucleosynthesis upon novae. In this context, whether the WD is a CO WD or an ONeMg WD is important for this thesis; a nova is called '**CO nova**' in the former case, and '**neon nova**'[9] (or 'ONe nova' or 'ONeMg nova') for the latter[10] For example, according to nucleosynthesis models of novae (Figure 1.2; Politano et al., 1995; José & Hernanz, 1998; José et al., 2006; Iliadis, 2015; José et al., 2020), aluminum is largely excessed only in neon nova models while not in CO nova models, because the Ne-Na and Mg-Al cycles (Boeltzig et al., 2016) work much more efficiently in the ONeMg WD case.

For most metals in the Universe, massive stars and supernovae have played important roles. However, for some isotopes novae do; novae have been considered to be an important source of some isotopes, such as ^{7}Li, ^{13}C, ^{15}N, ^{17}O, ^{22}Na, and ^{26}Al (Gehrz et al., 1998). Recently, explosive ^{7}Li production in novae has been observationally established (e.g., Tajitsu et al., 2015). ^{26}Al is famous for the 1.8 MeV nuclear γ-rays, which are observed along the Galactic plane and therefore considered to originate from star-forming regions (i.e., massive stars and supernovae) (Mahoney et al., 1982, 1984; Diehl et al., 1995, 2006). However, it has been reported that some grains have isotopic ratios of ^{26}Al/^{27}Al consistent with nova (on WDs having ONe cores) models (Amari et al., 2001) and that 1/3 of ^{26}Al in LMC is predicted to be produced by novae according to a recent chemical evolution model (Vasini et al., 2023). These examples show potentially important roles played in general by novae, and some unique roles by neon novae, in the origin of elements and isotopes.

Simply speaking, the unique environment of novae can be attributed to why novae are expected to contribute to cosmic chemistry in some isotopes. The important points are,

[9] As the name suggests, the observational classification as a neon nova is based on the overabundance of neon derived from neon lines, especially [Ne III] and [Ne V] in the decline (coronal) phase (e.g., Bode & Evans, 2008).

[10] Unlike CO novae, a He nova is not a nova on a He WD but a nova burning helium instead of hydrogen (see, e.g., Kato et al., 2023).

(1) Proton-rich: since protons are abundant in novae, nuclei grow up by proton-capture.

(2) Hotter and denser than main sequence stars: the timescale of the proton capture in novae tends to be shorter than that in main sequence stars, and even than the lifetime of some unstable nuclei (Figure 1.3, especially in 0.2 GK environment). Therefore, proton-rich nuclei can be overabundant. For example, not $^{14}\mathrm{N}(p,\gamma)^{15}\mathrm{O}$ (as in stars) but the β^+-decays of $^{13}\mathrm{N}$ and $^{15}\mathrm{O}$ limit the rate of the CNO-1 cycle, and most of the CNO nuclei become β^+-unstable (§4 of Bode & Evans, 2008, by Starrfield). The so-called hot CNO cycle ($^{13}\mathrm{C}(p,\gamma)^{14}\mathrm{O}$ and $^{14}\mathrm{N} + \mathrm{e}^+ + \nu_\mathrm{e}$) can be activated (Boeltzig et al., 2016). Also, the nuclear energy generation in TNR is limited by the β^+-decay (§4 of Bode & Evans, 2008). For the detail of hydrogen-burning, see e.g., `https://cococubed.com/code_pages/burn_hydrogen.shtml`.

(3) Ejective: the daughter nucleus can be escaped from the system as nova ejecta before being broken. It is especially important for $^7\mathrm{Li}$, which is easily broken by $^7\mathrm{Li}(p,\gamma)^8\mathrm{Be}$ and $^8\mathrm{Be} \to 2\alpha$. In novae, the proton-rich nuclei $^7\mathrm{Be}$, whose half-life time is 53.3 days (longer than or comparable to the typical timescale of novae[11]) is synthesized a lot (Tajitsu et al., 2015), and β^+-decays to $^7\mathrm{Li}$ after it is escaped.

1.5 Nova in the Hertzsprung-Russell Diagram

According to the simulations/theories of novae, the TNR occurs while the WD photosphere constant radius (e.g., Hillman et al., 2014; Kato et al., 2017). The timescale of TNR, minutes (see also (2) in §1.4), is shorter than that of dynamical expansion time (accorting to Hillman et al. 2014, it is hours to days). The expansion is finally possible when the luminosity has approached the Eddington limit,

$$L_\mathrm{Edd} = \frac{4\pi G M m_\mathrm{p} c}{\sigma_\mathrm{T}} \sim 3 \times 10^4 L_\odot, \tag{22}$$

where σ_T is Thomson's cross-section for electron scattering. Stars emitting photons more luminous than this luminosity are so bright that due to the strong radiation pressures they cannot have static structure. The point is, if the nuclear energy generation rate exceeds the Eddington limit, the radiation cannot bring all of them out; the radiation luminosity is limited by factors of Eddington luminosity, and the rest of the nuclear energy is spent for the expansion/outflow[12] (and internal energy) of the envelope. Therefore

[11] Compared to novae, many stars have long enough lifetimes for lithium to be transported by convection toward the center and be broken there.

[12] The gravitational potential plays an important role in absorbing excess nuclear energy beyond how much the photospheric emission releases (Kato et al., 2017). Note that, roughly estimated, the gravitation potential for a proton

$$\frac{G M_\mathrm{WD} m_\mathrm{p}}{R_\mathrm{WD}} = 0.22 \left(\frac{M_\mathrm{WD}}{M_\odot}\right)\left(\frac{R_\mathrm{WD}}{R_\oplus}\right)^{-1} \mathrm{MeV}, \tag{23}$$

is usually smaller than the typical expected nuclear energy release from a proton (7–8 MeV); therefore only a small fraction of hydrogen accreted is burnt; therefore a large fraction of hydrogen accreted is expected to escape.

the photosphere expands while the luminosity is almost constant, leading to the effective temperature decrease. Thereby the optical luminosity increases by orders (i.e., the bolometric correction decreases since the SED peak shifts from soft-X to the UV or optical).

Finally, the photosphere peaks around $\sim 10^2\ R_\odot$, and the system settles in a quasi-steady state with '**optically thick wind**' (Kato & Hachisu, 1994). The photosphere cannot be maintained such large as the mass that remains in the envelope decreases. Then, the photosphere reverses the trajectory; as the photosphere shrinks and the WD is exposed, it is observed as a **supersoft X-ray source** (SSS). After the nuclear reaction quenches, the photosphere is cooled down by radiation cooling.

This theoretical insight that initial brightenings in novae are attributed to decreasing effective temperature is having been proven observationally. Arai et al. (2015) took a spectrum of the recurrent nova T Pyx 0.19 days after the discovery of its 2011 outburst, during the initial brightening. Their spectrum, taken during initial brightening, shows highly ionized emission lines (e.g., He II, C IV, N III, and N IV). In 2020, eROSITA detected a short bright emission in a soft X-ray from the nova YZ Ret that ended before it brightened in the optical wavelength (König et al., 2022). These examples prove that there must be a high-temperature phase during or before the initial brightening phase of novae. In 2021, we observed the classical nova V1405 Cas 9.88 hours after the discovery and again confirmed highly-ionized emission lines only seen during the initial brightening phase (Chapter 3). Another important object in this context is the extremely slow nova Gaia22alz (Aydi et al., 2023; Brink et al., 2022) in 2022; its first spectrum, which was taken when it was only $\lesssim 4$ magnitude above its quiescent, resembled that of T Pyx in the existence of prominent Balmer, He I, He II, N III, and C IV lines, though it is an 'outlier' in the extremely slow light curve properties.

Theoretically[13] , it is generally accepted that novae with faster (slower) declines in the light curves are associated with heavier (lighter) WDs[14] (e.g., Kato & Hachisu, 1994; Hachisu & Kato, 2010). This relationship is understandable considering that nuclear reactions in the envelope and the expansion of the envelope support novae. The larger the $M_{\rm WD}$ is, the more intense the nuclear reactions are due to the higher density and the larger $M_{\rm env}$ is, therefore, the sooner the nova spends out hydrogen by nuclear reaction and wind.

[13] Also, note that the relationship has little evidence based on the direct measurement of $M_{\rm WD}$ (Chomiuk et al., 2021), though it is agreed that most neon novae are in this class that the ejecta velocities in fast novae are often larger than in slow novae (§3.2).

[14] While the WD mass is the main controlling factor, there are also other factors that affect the nova speed class (e.g., the accretion rate from the secondary star; Yaron et al., 2005).

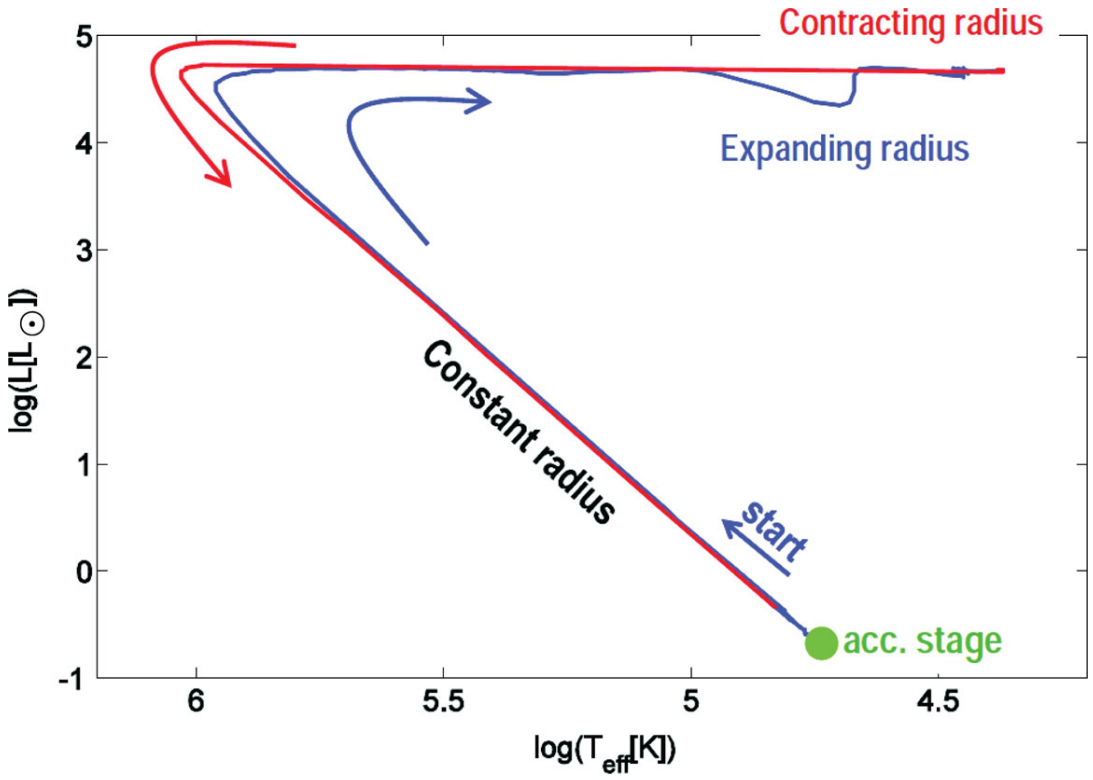

Figure 1.4: A 'nova cycle' model ($M_{\rm WD} = 1.25 M_{\odot}$, $T_{\rm c} = 5 \times 10^7$ K, and $\dot{M}_{\rm WD} = 1 \times 10^{-10}$ $M_{\odot}$/yr) drawn in the HR diagram. Adopted from Figure 1 in Hillman et al. (2014), "Nova multiwavelength light curves: predicting UV precursor flashes and pre-maximum halts".

1.6 The Structure of Thesis

As mentioned above, the early phases, especially the initial brightening phase, are important in understanding the physics of novae. However, very few objects have been observed in detail (e.g., spectroscopy). Nevertheless, thanks to the developments in transient surveys, we consider by using the Seimei telescope of Kyoto University, we can contribute to increasing such examples. In chapter 2, I briefly describe our observational program aiming for early spectra of classical novae. In chapter 3, the early spectra of the classical nova V1405 Cas are shown and discussed. The spectra do not only confirm that the photospheric temperature of the nova was high during the initial rise but also reveal this is a neon nova whose $M_{\rm WD}$ is smaller than the typical $M_{\rm WD}$ expected by single-star evolution models.

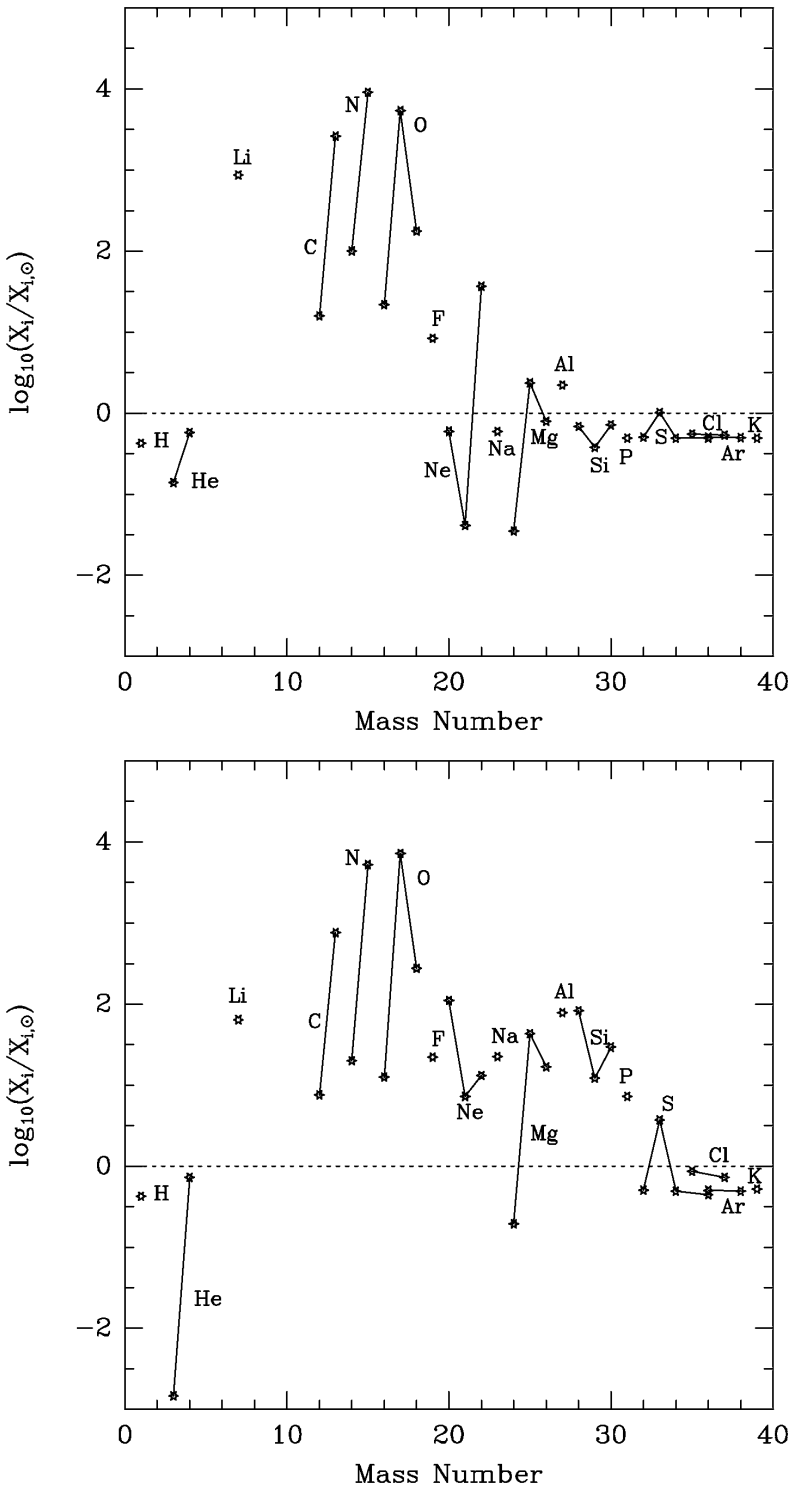

Figure 1.2: A comparison of overproduction factors (relative to solar) in the ejecta of $M_{\rm WD} = 1.15\ M_{\odot}$ models. (Top) CO nova model. (Bottom) ONe nova model. Adopted from Figures 2 and 3 from José et al. (2006), "Nucleosynthesis in classical novae".

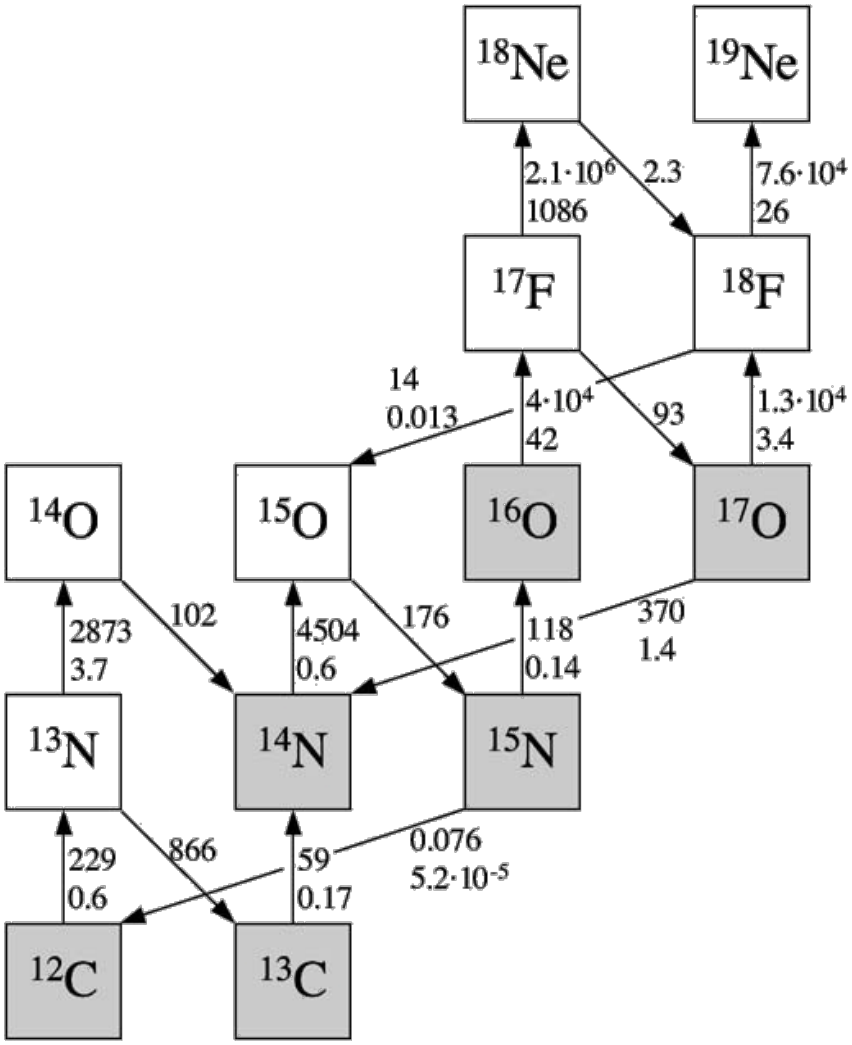

Figure 1.3: Nuclear reactions in CNO cycle 1and 2 and hot CNO cycle 1 and 2. For β^+-decays, the number next to the arrow represents the mean lifetime in seconds. For nuclear reactions, the upper and lower number next to the arrow represent the mean reaction lifetime in seconds for $\rho = 200$ g/cm^3 and $X_{\rm H}/A_{\rm H} = 1$, at a temperature of 0.1 (top) and 0.2 (bottom) GK, respectively. Adopted from Figure 1 in José et al. (2006), "Nucleosynthesis in classical novae".

Chapter 2

Our Observational Program of Novae for Initial Phase

Theoretically, the temperature of the photosphere of novae during its initial rise has long been considered to be high (§1.5), providing a different condition for spectral formation as compared to the later, well-observed epochs. Therefore, spectroscopic observations in such an infant phase are expected to provide new insight into the natures of the WD progenitor and the ejecta dynamics just after the initiation of the thermonuclear runaway. By increasing the number of novae well-observed in these phases, the early expansion/ejection of the H-rich envelope and the state of the system just before the nova eruption are expected to be understood better; without such observations (i.e., only by observations after the initial brightening phase ends), we can only observe the system after the later ejected material has been dominant.On the other hand, the spectrum of T Pyx during the initial rising Arai et al. (2015) does not show the absorption component of the P Cygni profile, as most nova spectra around the peak magnitudes show, and it has possibly not been affected by such material; considering their spectrum and that the photosphere expands during the initial rise (§1.5), we can naturally have the following depiction (Figure 2.1):

Stage 1 (Early Initial Brightening Stage):

Since the radius of the photosphere is very small on this stage, a very high photospheric temperature is expected. The photospheric temperature keeps decreasing, following the photospheric expansion. Only a negligible fraction of ejecta is exposed outside the photosphere, and therefore the ejecta hardly contribute to the formation of spectral lines. Especially, the P Cygni absorption components are not expected to be formed yet. Instead, materials that have existed around the system since before the nova explosion (circum stellar material; **CSM**) may show prominent emission lines if there are, since they are expected not to have been yet swallowed by the dense nova ejecta.

Stage 2 (Late Initial Brightening Stage):

The photosphere starts receding inward in the mass coordinate (Figure 2.1). In other words, the expansion of the photosphere in the radial coordinate starts decelerating. The amount of the ejecta material outside the photosphere increases as time goes by, leading to the formation of spectral lines by such ejecta material itself[15]. Therefore, the lines are expected to show the P Cygni profiles from this stage, unlike stage 1. The photospheric radius must be much smaller than in the maximum light or pre-maximum halt (stage 3), and thus the photospheric temperature is still high and it decreases as time goes by. Within the ejecta, outer materials probably have a higher outward velocity, and thus the recession of the photosphere in the mass coordinate is followed by the decrease in the absorption velocity of the P Cygni profiles (Figure 2.1, Aydi et al., 2020).

Stage 3 (After Initial Brightening Stage: pre-maximum halt or maximum):

The spectral formation is characterized by a low photospheric temperature and the P Cygni profile[15]. Most of the 'early' nova spectra reported so far have been taken in this stage.

[15]If there remains enough dense material outside the ejecta front (though it is not seen in Figure 2.1), the possibility that they can be detected cannot be ruled out (Figures 2.2, 2.3).

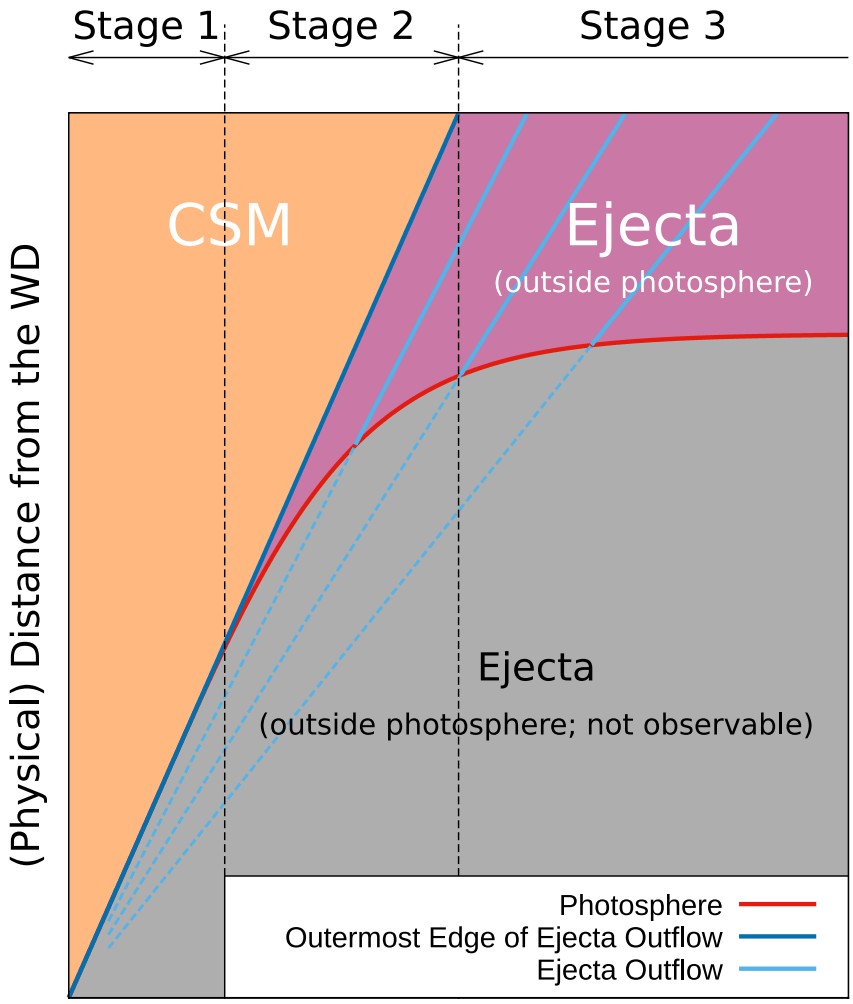

Figure 2.1: Qualitative diagram of the nova outflow and photosphere in the early stage. The cyan and blue lines are the trajectory of the ejecta outflow and its front, respectively. These lines are also the trajectory of the mass coordinate. The red line shows the size of the photosphere, inside of which (the gray area) cannot be observed. The magenta and orange regions correspond to where the nova outflow has and has not reached, respectively. The upper axis shows the relationship between stages in the text and the evolution of the nova.

Also, γ-rays from novae have been reported recently (since the Fermi-LAT age; e.g., Abdo et al., 2010), which leads to attention on shock acceleration in novae. Very recently, TeV γ-rays from the recurrent nova RS Oph in 2021 were detected by H.E.S.S. (H. E. S. S. Collaboration et al., 2022). This is considered due to the massive wind from the secondary star has surrounded the system prior to the nova outburst (note that this system is symbiotic and the secondary star is giant). In fact, narrow emission lines, probably originated from the wind, were observed strongly in the optical wavelength for a long time (Figures 2.2, 2.3).

The initial ejection of a nova has been in attention not only because it makes shock waves but also

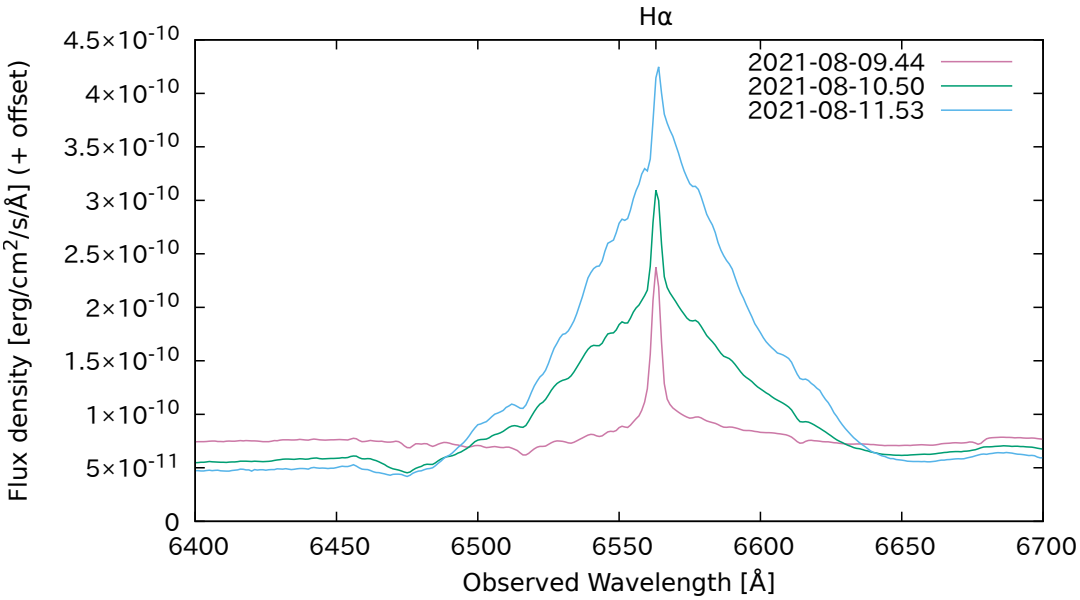

Figure 2.2: Spectra around Halpha line of the recurrent nova RS Oph in the early epochs of its 2021 outburst (Taguchi et al., 2021l,i). Though a broad emission component attributed to the ejecta dominates, a narrow emission component also seen which is most likely from the dense wind from the secondary outside the ejecta front.

because its mass[16] determines the fate of the binary star system. For example, the amount of nova ejecta determines whether the WD finally reaches the Chandrasekhar mass ($M_{\rm Ch}$) to hold a type-Ia supernova (SN Ia) or not; if the amount of mass accretion between two nova outbursts next to each other exceeds the amount of mass ejection by the nova explosion, $M_{\rm WD}$ should increase. Therefore, it is important to measure the amount of nova ejecta precisely (especially in fast novae, whose $M_{\rm WD}$ is close to $M_{\rm Ch}$ and whose main mass-ejection phase ends immediately).

Another potential benefit that could be added by such a prompt spectroscopic observation, as we demonstrate in chapter 3, is the nature of a progenitor WD. Depending on their internal chemical composition, WDs are largely divided into two types, CO WDs and ONeMg WDs (§1.1) and novae are into CO novae and neon novae (§1.4). However, it is usually difficult to determine their nature either as a CO WD or ONeMg WD by observing 'static' WDs, since the internal composition is hidden by a layer of H or He on the surface and is observed just as DA or DB WD, respectively. A nova provides an interesting alternative opportunity; the nature of the underlying WD can be inferred either as a CO WD or ONeMg WD, through the spectral identification, i.e., CO nova for the former and neon nova for the latter[9]. Further, it is possible to estimate the WD mass behind a nova, since the 'speed class', i.e., fast (slow) novae are associated with high-mass (low-mass) WDs (§1.5).

[16]This is also difficult for hydrodynamical simulations to study; since the H-envelope is geometrically thin and the ejecta velocity is as fast as ~ 1000 km s^{-1}, the time step should be small to satisfy the Coulant condition.

However, it is an extremely challenging observation, given the short time scale associated with the initial brightening. Nevertheless, Arai et al. (2015) reported such a prompt spectroscopic observation of the recurrent nova T Pyx in its 2011 outburst (§1.5). As they demonstrated following-up observation of novae in the initial phase has been becoming possible nowadays. Especially, the high-cadence surveys like All Sky Automated Survey for SuperNovae (ASAS-SN, Shappee et al., 2014), Zwicky Transient Facility (ZTF, Bellm et al., 2019), Tomo-e Gozen (Sako et al., 2018), and Palomar Gattini-IR (Moore et al., 2016; De et al., 2020) have been evolved a lot. Therefore, we have been expecting that we can increase the number of such examples with an appropriate system well-prepared rather than hoping for tremendous luck and doing nothing. In order to perform follow-up spectroscopic observations of novae in the initial phases, we have been running a follow-up observation program targeting novae using the 3.8 m Seimei telescope (Kurita et al., 2020) of Kyoto University since 2019, when this telescope started operation. The telescope provides the best environment for such observation; its pointing is fast, light-gathering power is strong[17], and Time-of-Opportunity (ToO) observations are allowed to interrupt other observations. Through this program, we have followed young nova 'candidates'; some are not novae but other transients like dwarf novae, which rise by smaller amplitude than novae; however, not to miss initial nova candidates, we have triggered candidates which have non-negligible nova probability[18]. We have expected one Galactic nova to start when it is observable night from Okayama in 2 or 3 years[19].

The basic scheme is the following. Our targets are Galactic novae and novae in M31. In both cases, the limiting magnitude is $\sim$ 18.5 AB mag. For Galactic novae, the peak magnitudes are from naked-eye visibility to close to the limit, depending on the distance and Galactic extinction. For novae in M31, the peak magnitudes are typically between 16.5 and 18.5 for less-extinct ones. In principle, we select targets considering their positions and magnitudes to exclude candidates that are less likely novae. However, we have actively triggered our program for these candidates if they are just after the discovery (the amplitude is to be larger) and if the telescope is free (e.g., under the Director's Discretionary Time unallocated or the sky is in twilight). We start with the low-resolution VPH-blue grism to see the overall features. Within a few minutes for brighter targets or an hour for fainter targets, we can judge whether the ongoing target is likely a nova in initial brightening or not (nova after initial brightening or non-nova) by checking the presence/absence of highly-ionized emission lines from the Quick Look file automatically generated by KOOLS-IFU control server. If the object is not a nova in initial brightening, we terminate our observation there. If the target is the very a nova in initial brightening, we keep taking data until the elevation gets too low or the background is too bright. Finally, we have managed to observe V1405

[17]It enables us to take not only a high S/N ratio but also high time-resolution data because it saves the single exposure time required.

[18]In the four years, we have 'learned'; the probability we triggered our program for non-nova transients has decreased little by little.

[19]Roughly estimated, considering the probabilities of whether a nova is in the northern hemisphere or not (1/2), whether a nova is close to the sun (1/2), if Okayama is night or not when nova ignites (1/2), and the clear sky rate (1/3), one of 20–30 novae can be a golden target. Considering the event rate of Galactic novae, $\sim$ 10 yr^{-1}, we expect one golden target in 2–3 years. Here we neglect the probability transient surveys miss the target; we expect the surveys 'perfect'.

Cas (chapter 3) during its initial rise[20] throuhgh this program. Our past targets are listed in Table 2.1.

[20] We could have been able to observe other targets if the condition allowed; we gave up V1674 Her by the weather condition and U Sco by the lack of a 'local' observer who had been required to perform 'remote' ToO then.

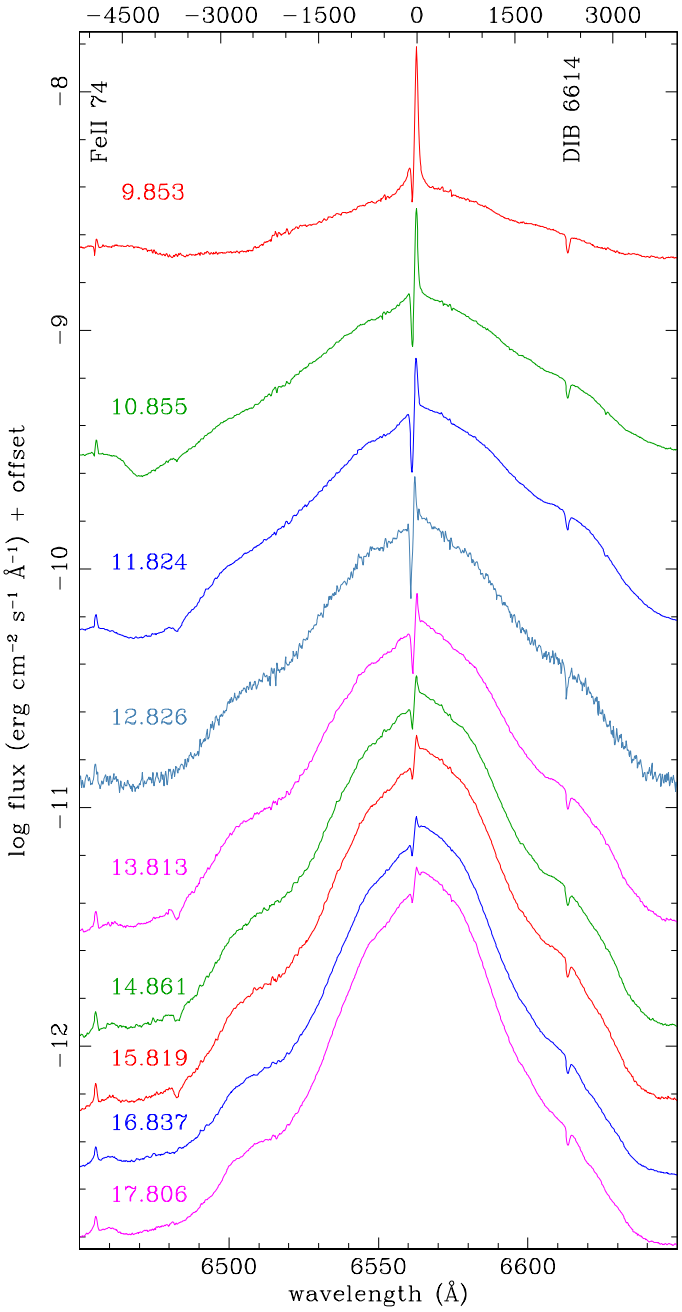

Figure 2.3: The same as Figure 2.2 but high-resolution spectra. Thanks to the high resolution, the narrow component is also seen in the P Cygni profile. Adopted from Figure 4 in Munari & Valisa (2021), "The 2021 outburst of RS Oph. A pictorial atlas of the spectroscopic evolution: the first 18 days".

Table 2.1: Observed targets by the Seimei telescope by our program or related programs.

Object	References	Classification
V670 Ser	Taguchi & Maehara (2020)	nova
ZTF20aavnpug	Isogai & Maehara (2020)	dwarf nova
TCP J20034647+1335125	Taguchi et al. (2020c)	dwarf nova
ASASSN-20kv	Taguchi & Isogai (2020)	dwarf nova
ASASSN-20kw	Taguchi et al. (2020d)	dwarf nova
MASTER OT J213908.79+161240.2	Isogai et al. (2020)	dwarf nova
ASASSN-20mf	Isogai et al. (2020)	dwarf nova
ASASSN-20om	Taguchi et al. (2020b)	nova in M31
ZTF20acufmah	Taguchi et al. (2020a)	dwarf nova
PNV J00494338+4033383	Taguchi et al. (2020e)	dwarf nova
PNV J00425220+4116246	Taguchi et al. (2021d)	nova in M31
PNV J00434645+4133408	Taguchi et al. (2021d)	nova in M31
TCP J10203579+3103424	Taguchi et al. (2021m)	dwarf nova
ASASSN-21au	Isogai et al. (2021)	helium dwarf nova
PNV J00420424+4042336	Taguchi et al. (2021n)	nova in M31
PNV J00434013+4127123	Taguchi et al. (2021a)	nova in M31
V1405 Cas	Maehara et al. (2021)	nova
V6595 Sgr	Taguchi & Isogai (2021a)	nova
PGIR21fjn/AT2021kgk	Taguchi & Isogai (2021b)	nova
ASASSN-21gq	Taguchi et al. (2021c)	microlensing
TCP J18224935-2408280	Taguchi et al. (2021h)	symbiotic star
RS Oph	Taguchi et al. (2021l)	nova
PNV J00444033+4113068	Taguchi & Maehara (2021)	dwarf nova
TCP J17242302+3258109	Taguchi et al. (2021b)	dwarf nova
M31N 2008-12a	Taguchi et al. (2021g)	recurrent nova in M31
Gaia21efs	Taguchi et al. (2021f)	microlens
MASTER OT J030227.28+191754.5	Taguchi et al. (2021k)	dwarf nova
AT 2022cpe	Taguchi & Yamanaka (2022)	nova in M31
U Sco	Taguchi et al. (2022b)	nova
GDS J1830235-135539	Taguchi et al. (2022a)	symbiotic nova
ASASSN-22lk	Taguchi et al. (2022a)	dwarf nova
AT 2022yok	Maeda et al. (2022)	dwarf nova
AT 2022zyr	Taguchi & Otsuka (2022)	M31
AT 2022aavm	Taguchi (2022)	dwarf nova
PNV J00215475+5231007	Taguchi (2023a)	dwarf nova
AT 2023nf	Taguchi et al. (2023d)	dwarf nova
V6596 Sgr	Taguchi (2023b)	nova
AT 2022abzg	Taguchi (2023c)	nova in M31
V6597 Sgr	Taguchi (2023d)	nova
AT 2023hwu	Taguchi (2023e)	dwarf nova
AT 2023ivk	Taguchi et al. (2023b)	dwarf nova
TCP J19183710+2127170	Taguchi et al. (2023a)	young stellar object
AT 2023srv	Taguchi & Maeda (2023)	dwarf nova
AT 2023oom	Taguchi (2023f)	nova in M31
AT 2023ttu	Taguchi (2023g)	nova in M31
TCP J18433189+1011051	Taguchi et al. (2023c)	dwarf nova
AT 2023ufj	Taguchi et al. (2023e)	nova in M31

Chapter 3

Spectra of V1405 Cas (= Nova Cassiopeiae 2021) at the very beginning indicate a low-mass ONeMg white dwarf progenitor (Taguchi et al., 2023f)

3.1 Abstract

The lowest possible mass of ONeMg WDs has not been clarified despite its importance in the formation and evolution of WDs. We tackle this issue by studying the properties of V1405 Cas (Nova Cassiopeiae 2021), which is an outlier given a combination of its very slow light-curve evolution and the recently reported neon-nova identification. We report its rapid spectral evolution in the initial phase, covering 9.88, 23.77, 33.94, 53.53, 71.79, and 81.90 hours after the discovery. The first spectrum is characterized by lines from highly-ionized species, most noticeably He II and N III. These lines are quickly replaced by lower-ionization lines, e.g., N II, Si II, and O I. In addition, Al II (6237 Å) starts emerging as an emission line at the second epoch. We perform emission-line strength diagnostics, showing that the density and temperature quickly decrease toward later epochs. This behavior, together with the decreasing velocity seen in Hα, Hβ, and He I, indicates that the initial nova dynamics is reasonably well described by an expanding fireball on top of an expanding photosphere. Interestingly, the strengths of the N III and Al II indicate large abundance enhancement, pointing to an ONeMg WD progenitor as is consistent with

its neon-nova classification. Given its low-mass nature inferred by the slow light-curve evolution and relatively narrow emission lines, it provides a challenge to the stellar evolution theory that predicts the lower limit of the ONeMg WD mass being $\sim 1.1\ M_{\odot}$.

3.2 Introduction

Theoretically, the temperature is considered to be high in the initial phase (§1.5), which provides a different condition for spectral formation as compared to the later, well-observed epochs. Therefore, spectroscopic observations in such an infant phase are expected to provide new insight into the natures of the WD progenitor and the ejecta dynamics just after the initiation of the thermonuclear runaway. However, it is an extremely challenging observation, given the short time scale associated with the initial brightening (chapter 2); except for some symbiotic novae or extremely slow novae, e.g., Gaia22alz (Aydi et al., 2023; Brink et al., 2022), only a single example, the recurrent nova T Pyx in its 2011 outburst, has been reported for such a prompt spectroscopic observation (Arai et al., 2015).

As described in chapter 2, another potential benefit that could be added by such a prompt spectroscopic observation, as we demonstrate in the present chapter, is the nature of a progenitor WD; by observing nova spectra and nova light curves, we are able to infer the chemical composition (i.e., CO or ONeMg) and mass of the WD. Especially interesting in this context is the mass range for ONeMg WDs. Compared to CO WDs, ONeMg WDs are predicted to be generally more massive, as they are end products of more massive stars (§1.1). Theoretically, the minimal mass of ONeMg WDs has long been studied by stellar evolution simulations (e.g., Nomoto, 1984; Iben & Tutukov, 1985; Nomoto, 1987). According to a recent study (Lauffer et al., 2018), it is $\sim 1.1\ M_{\odot}$. However, there are some observational works that challenge this picture, and the minimal mass of ONeMg WDs has not been clarified. For example, Kepler et al. (2016) reported a discovery of an ONeMg WD with $0.56 \pm 0.09\ M_{\odot}$. Observations of novae can form potentially important data sets to tackle this issue, as the WD composition and the mass can be connected for individual objects.

Neon novae almost exclusively belong to fast or very fast novae[21] (Bode & Evans, 2008) and are therefore associated with a massive ONeMg WD. This picture was however challenged by the discovery of a slow *and* neon nova – Takeda et al. (2018) concluded the very slow nova V723 Cas (Nova Cassiopeiae 1995) is a neon nova, hosting a WD of only $\sim 0.6\ M_{\odot}$. To further investigate the mass range of ONeMg WDs (especially toward the low-mass end), an additional support of an ONeMg WD progenitor for a slow nova that shows potential signatures of a neon nova will provide an important step.

In this chapter, we show the result of our follow-up spectroscopy of the very slow nova V1405 Cas which was recently reported to be a neon nova based on its spectra in the decay phase (Munari &

[21] The opposite is not the case, i.e., there are many CO novae showing fast light curves, e.g., the recurrent novae V3890 Sgr (Orio et al., 2020) and RS Oph (Mikołajewska & Shara, 2017).

Valisa, 2022), i.e., the second example of a very slow nova categorized as a neon nova. We present very early-phase spectral evolution soon after the discovery, including a spectrum taken during the initial rise, and report the detection of Al II λ6237 and Al III $\lambda\lambda$ 5697/5723. We perform line-strength diagnostics that shows overabundances of aluminum, suggesting that the progenitor WD is indeed an ONeMg WD despite its likely low mass nature in view of the slow light-curve evolution. This chapter is structured as follows. We describe the basic properties of V1405 Cas in §3.3. Our observations and data reductions are shown in §3.4, where we also describe overall spectral evolution. In §3.5, we diagnose the physical condition of the system from the line strengths (some details are in Appendix A). In §3.6.1, we discuss the possibility that V1405 Cas is a low-mass ONeMg WD. In §3.6.2, we discuss the possible correlation between aluminum overabundance and neon novae. In §3.6.3, we discuss how Al II λ6237 can be used as the earliest indicator to identify neon nova candidates that may help coordinate intensive observations for similar events in the future. We conclude this chapter in §3.7.

3.3 Basic Properties of V1405 Cas

V1405 Cas (= Nova Cassiopeiae 2021 = PNV J23244760+6111140) was discovered as a transient candidate by Yuji Nakamura at 9.6 mag (unfiltered) on 2021-03-18.4236 UT (JD 2459291.9236)[22]. Hereafter, we denote t as the time measured from the discovery time by Nakamura[23]. It was then confirmed as a classical nova (Maehara et al., 2021; Taguchi et al., 2021j), who reported the first spectrum shown in the present chapter.

The position of the nova coincides with a Gaia Data Release 3 (Gaia Collaboration et al., 2016, 2022) source (2015451512907540480), which is characterized by an average G magnitude = 15.36 and a parallax p = 0.5776103855139701 ± 0.025421817 mas. Hereafter, we adopt d = 1.73 $^{+0.08}_{-0.07}$ kpc as the distance to the nova, as inferred from the Gaia parallax. Taking the color[24] and Gaia distance into account, the progenitor is most likely a nova-like variable (Taguchi et al., 2021j; Schaefer, 2021). Recently, Schaefer (2021) derived its orbital period of 0.1883907 ± 0.0000048 days from the TESS data (Ricker et al., 2015) taken before the outburst (see also the Czech Variable Star Catalogue[25]; Skarka et al., 2017).

V1405 Cas initially showed He/N type spectra, but after a month it started to show Fe II type spectra (Shore et al., 2021b; Munari et al., 2021a). After that, following the luminosity decrease, it showed He/N type spectra again (Shore et al., 2021a). Finally, based on the detection of overwhelming neon lines at t = +618 days, it was classified as a neon nova (Munari & Valisa, 2022).

[22] http://cbat.eps.harvard.edu/unconf/followups/J23244760+6111140.html

[23] While S. Korotkiy et al. reported to CBAT[22] that the system was seen at 13.53 ± 0.10 mag (unfiltered) on 2021-03-14.71017 (t = −3.7134 days), by the New Milky Way (NMW) survey (http://scan.sai.msu.ru/nmw/), this is far below the maximum magnitude.

[24] In addition to the Gaia Data Release 3, the Pan-STARRS1 Database (Flewelling et al., 2020) also records a source PS1 181423511988865624 at the position consistent with the nova. The PS1 magnitudes were g = 15.67, r = 15.46, i = 15.44, z = 15.36, and y = 15.32.

[25] http://var2.astro.cz/czev.php?id=3217.

From the light-curve evolution, V1405 Cas can be classified as a very slow nova. Since May 2021, V1405 Cas exhibited a seven-month plateau during which it repeatedly showed increases and decreases in its magnitude, whose amplitude reached 2–3 magnitudes (Figure 3.1). Such a light curve is similar to those of slow novae, including V723 Cas (Iijima et al., 1998; Iijima, 2006), HR Del (Rafanelli & Rosino, 1978), V1819 Cyg (Whitney & Clayton, 1989), and V5558 Sgr (Tanaka et al., 2011; Poggiani, 2008).

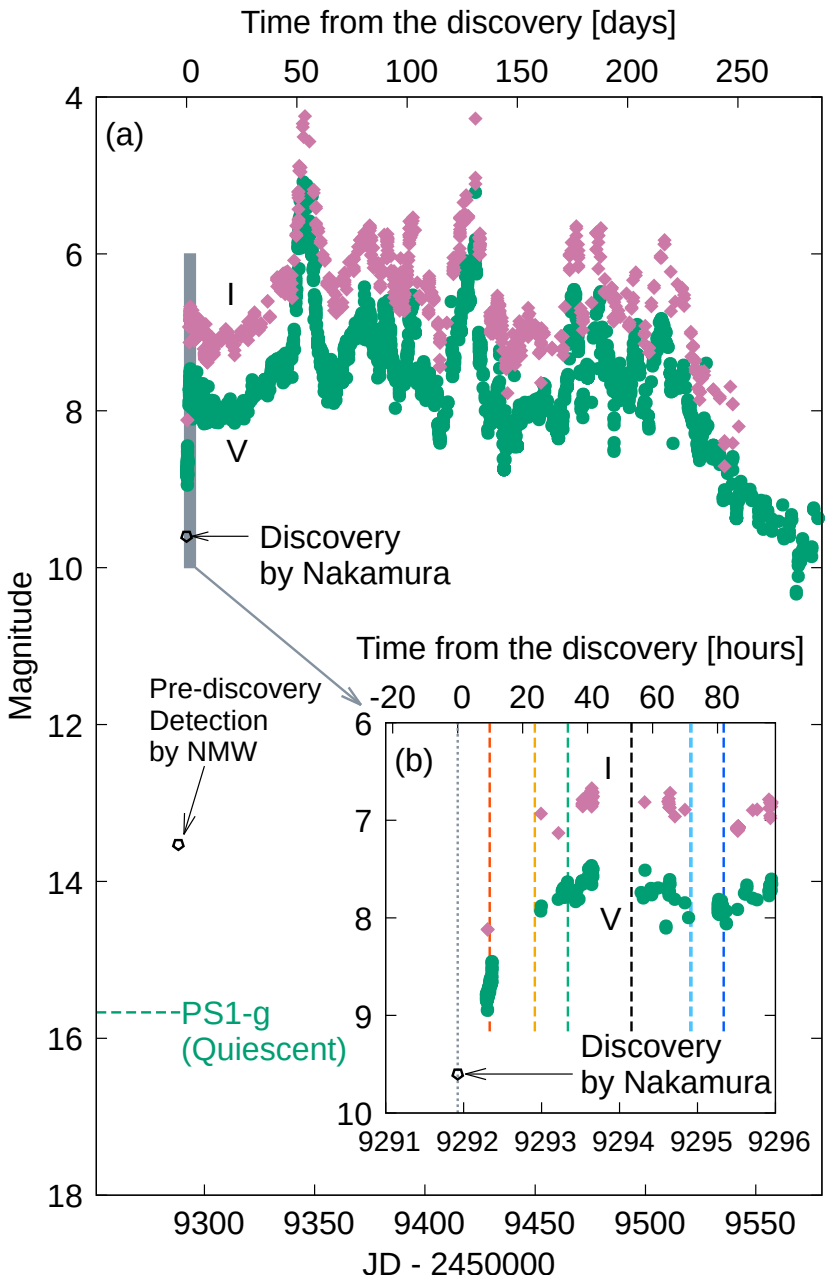

Figure 3.1: The light curves of V1405 Cas. (a) V and I magnitudes provided by AAVSO are shown by the green-filled circles and magenta-filled diamonds, respectively. The black open pentagons show the pre-discovery magnitude by the NMW survey and the discovery magnitude by Nakamura. (b) An enlarged view of the initial phase ($2459291 < \mathrm{JD} < 2459296$, the shaded region in the panel a. The dashed lines show the epochs of spectroscopic observations listed in Table 3.1, with the same color coordinate used to show our spectra in Figures 3.2 and 3.4.

3.4 Spectral Properties of V1405 Cas in the Very Early Phase

3.4.1 Observations and Data Reduction

We performed optical spectroscopy of V1405 Cas using the fiber-fed integral field spectrograph (KOOLS-IFU; Matsubayashi et al., 2019) on the 3.8-m Seimei telescope (Kurita et al., 2020) at Okayama Observatory, Kyoto University. The data were taken under the programs 21A-N-CT06 and 21A-K-0017. We used VPH-blue, VPH-red, and VPH683 grisms, which cover 4000 – 8900 Å, 5800 – 10200 Å, and 5800 – 8000 Å with the spectral resolution of $\sim$ 500, $\sim$ 800, and $\sim$ 2000, respectively.

Bias subtraction was performed using IRAF[26] in the standard manner. The gain correction was performed using software developed for KOOLS-IFU data. Spectra for all the fibers were reduced using the Hydra package (Barden et al., 1994; Barden & Armandroff, 1995), within which we used Hg, Ne, and Xe arc lamps for wavelength calibration. The typical accuracy of our wavelength calibration is $\lesssim$ 0.5 Å for VPH-blue and VPH-red, and $\lesssim$ 0.1 Å for VPH683. The characteristics in the optical properties for different fibers are corrected for by using twilight flat frames. For each frame, the sky subtraction was performed using the fibers in which the contribution from the target is negligible. After the sky subtraction, the fibers for V1405 Cas were selected and combined. We performed this spectrum combination separately in different wavelength ranges to correct for the atmospheric dispersion. For all the three grisms, the patterns of the wavelength dependence of count values specific to KOOLS-IFU were corrected for, with the standard star HR 7596.

Additionally, a high-resolution spectrum of V1405 Cas was obtained using the High Dispersion Spectrograph (HDS; Noguchi et al., 2002) attached to the 8.2 m Subaru Telescope on 2021 March 20 (t = 53.53 hours). The configuration was set to cover the wavelength region from 4030 to 6780 Å. We used 0.45 arcsec slit width, resulting in the spectral resolution of R $\simeq$ 80,000. For the wavelength calibration, we used Th-Ar comparison lamp with a typical error of $< 10^{-3}$ Å. Extraction of the spectrum in each order was carried out using the IRAF software in a standard manner (e.g., Tajitsu et al., 2010). The blaze functions for some echelle orders are difficult to derive directly, when broad lines are present within the order. We first created the blase functions for orders not containing such broad line features. Then, for the remaining orders, we interpolate the blaze functions from the orders that are located in the neighboring places in the 2D image, as they should share the similar blaze functions. The resulting blaze functions are then used to connect the spectra at different echelle orders, resulting in the final single flux-normalized spectrum.

The journal of our spectroscopic observations is shown in Table 3.1. The epochs of our spectroscopic observations are indicated in Figure 3.1. We emphasize that the initial brightening had not finished when we performed our first spectroscopy, given V = 8.460 on 2021-03-18.8465 (t = +10.24 hours) obtained

[26]IRAF is distributed by the National Optical Astronomy Observatories, which are operated by the Associations of Univesities for Research in Astronomy, Inc., under cooperative agreement with the National Science Foundation.

Table 3.1: The log of our spectroscopic observations. t is the time relative to the discovery time by Nakamura (JD = 2459291.9236).

Start	End	t [hours]	Airmass	Total Exposure Time [s]	
			(start – end)	(VPH-blue, red, 683)	(HDS)
2021-03-18.8196	2021-03-18.8509	+9.88	2.542 – 2.138	1680, 180, 240	–
2021-03-19.4095	2021-03-19.4187	+23.77	2.566 – 2.704	120, 180, 0	–
2021-03-19.8242	2021-03-19.8514	+33.94	2.434 – 2.098	1080, 150, 300	–
2021-03-20.6534	2021-03-20.6565	+53.53	3.6396 – 3.5286	–	180
2021-03-21.4123	2021-03-21.4178	+71.79	2.701 – 2.789	150, 120, 0	–
2021-03-21.8318	2021-03-21.8378	+81.90	2.259 – 2.162	180, 150, 180	–

by our simultaneous photometric observation using the 0.4-m telescope at Kyoto University (Taguchi et al., 2021j).

Figure 3.2 shows the overall view of our spectra with the flux scale normalized by the underlying continuum. Also shown are enlarged views around the wavelength ranges of interest (§3.4.2). To assist comparison with the KOOLS-IFU spectra, the HDS spectrum was resolution-decreased by convolving a Gaussian function of $\sigma = 100$ pixels and then down-sampled. Figure 3.3 shows enlarged views of the HDS spectrum, supporting line identifications (§3.4.3). Figure 3.4 expands the blue-shifted wings of Hβ and He I (7065Å).

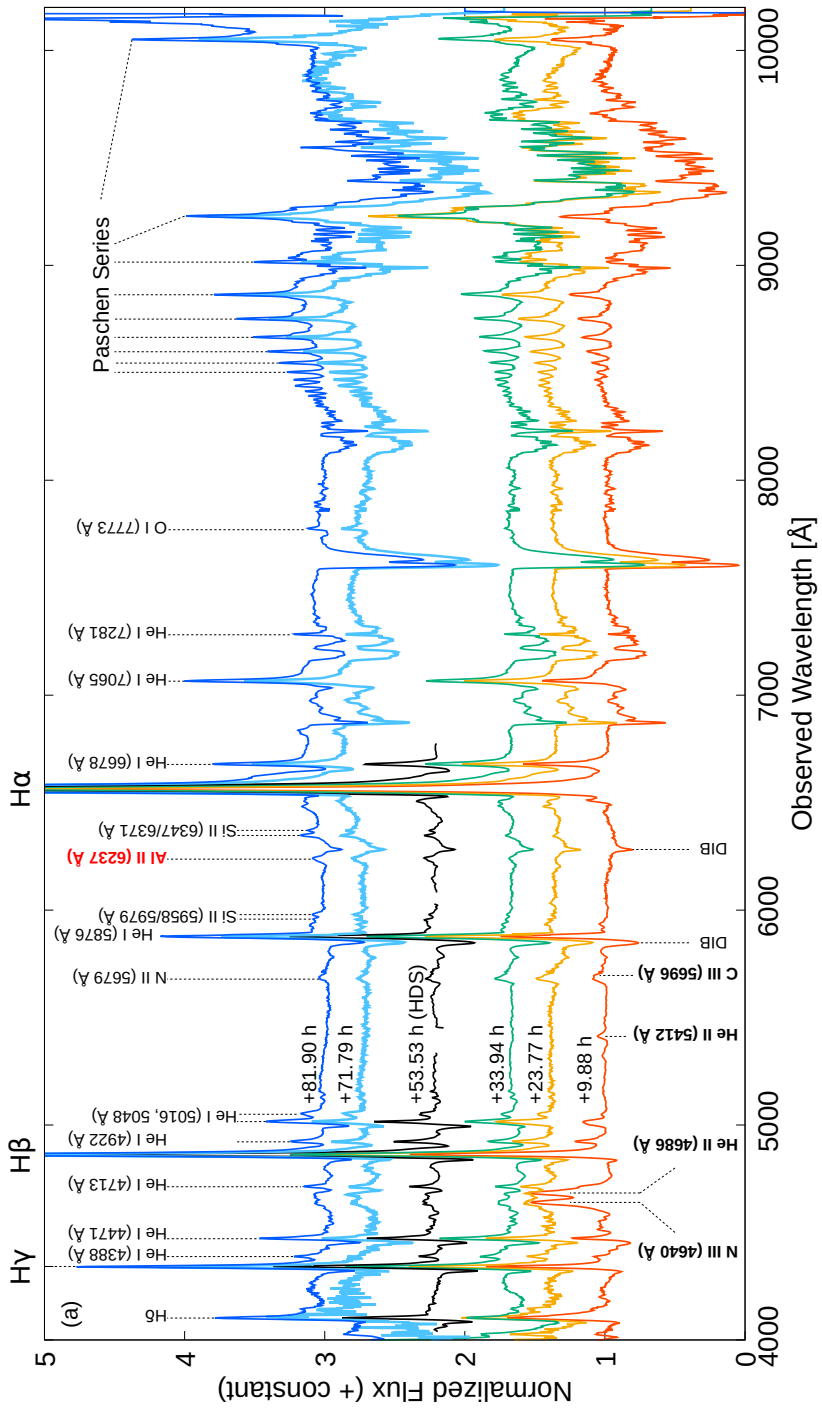

Figure 3.2: Spectra of V1405 Cas by the two low-dispersion grisms (VPH-blue and VPH-red, connected at 6050 Å) of KOOLS-IFU on t = +9.88, 23.77, 33.94, 71.79 and 81.90 hours, and by HDS (with the resolution artificially decreased to the KOOLS-IFU level, §3.4.1) on t = +53.53 hours. (a) An overall view of the normalized spectra. The lines labeled by the bold black font (He II, C III, and N III) are observed only at t = +9.88 hours. The Al II line labeled by the bold red font is one of the most striking lines discussed in §3.4.3.3, 3.5, and 3.6. (*continued on the next page*)

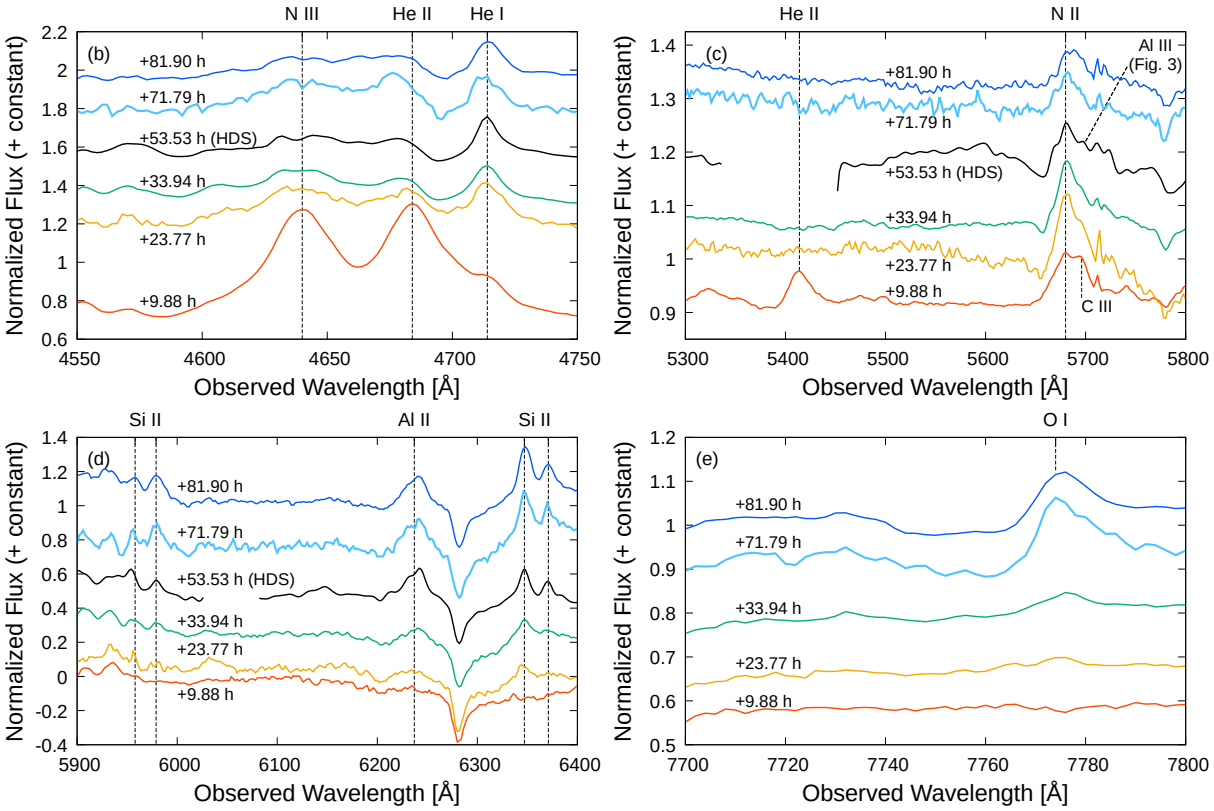

Figure 3.2 (Continued): (b, c, d, e) Enlarged views of the spectra shown in panel (a).

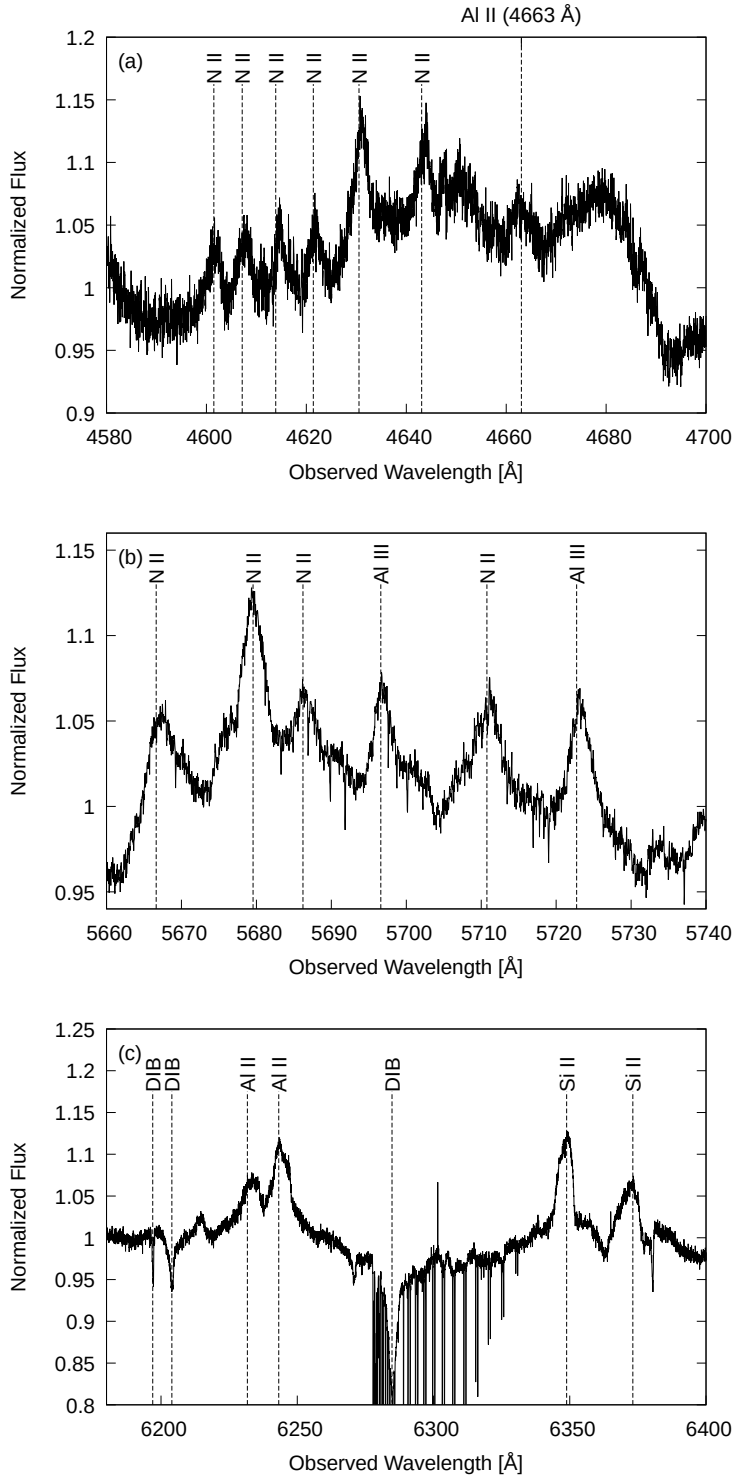

Figure 3.3: Enlarged views of the HDS spectrum on t = +53.53 hours. (a) 4580 – 4700 Å (§3.4.3.1). (b) 5660 – 5740 Å (§3.4.3.2). (c) 6180 – 6400 Å (§3.4.3.3).

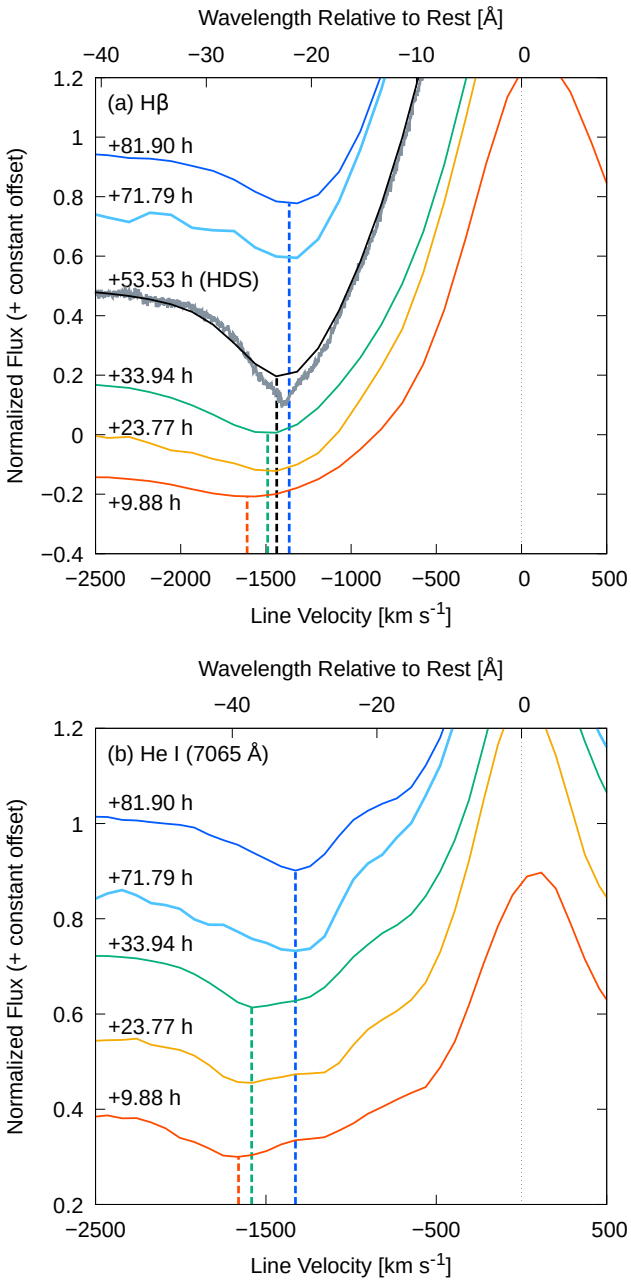

Figure 3.4: Profiles of the Hβ and He I (7065 Å) lines of V1405 Cas. In each panel, the absorption minima at several epochs, measured using the SPLOT task of IRAF, are indicated by dashed lines. (a) Spectra around the Hβ line obtained with the VPH-blue grism of KOOLS-IFU and with HDS. The absorption minima on $t = +9.88$, $+33.94$, and $+81.90$ hours are at $-1.6(1)$, $-1.4(9)$, and $-1.3(6) \times 10^3$ km s^{-1}, respectively. For the HDS spectrum ($t = +53.53$ hours), the original high-resolution spectrum (gray) and the resolution-decreased one (black; same as Figure 3.2) are overplotted. (b) The same as panel (a), but for the He I (7065 Å) line obtained using the VPH-red grism. The absorption minima on $t = +9.88$, $+33.94$, and $+$ 81.90 hours are at $-1.6(6)$, $-1.5(8)$, and $-1.3(3) \times 10^3$ km s^{-1}, respectively.

Table 3.2: Observed line luminosities measured using SPLOT task of IRAF in units of 10^{34} erg s^{-1}.

	t = +9.88 hours	t = +33.94 hours	t = +81.90 hours
Hα	17	50	50
Hβ	11	30	20
He I λ5876	2	14	9
He II λ4686	6	_[28]	_[28]
C III λ5696	0.14	–	–
N II λ5679	0.48	2.2	2.8
N III λ4640	8[31]	_[28]	_[28]
O I λ7773	–	0.04	0.15
Al II λ6237	–	0.3	0.12
Si II $\lambda\lambda$6347/6371	–	1	0.9

3.4.2 Summary of Evolution of the Spectral Lines

On all the epochs shown in the present chapter, the H I Balmer, Paschen, and He I lines are detected while Fe II lines are not (Figure 3.2a). The spectra of V1405 Cas, during the initial phase as presented here, thus show characteristics close to those of He/N type novae rather than Fe II type ones (Williams, 1992, 2012; Taguchi et al., 2021e)[27].

Notably, the strong lines of N III (4638 Å) and He II (4686 Å and 5412 Å) were detected only at t = +9.88 hours (Figure 3.2b, c). The spectrum, in which the N III triplet (4638 Å) is detected but N IV lines (e.g., 4058 Å, 7109–7123 Å) are not, is similar to those of late O-type stars (Gray & Corbally, 2009), which are characterized by high-ionization lines due to high temperature. Also, the C III line (5696 Å), overlapping with the N II line (5679 Å), is detected only at t = +9.88 hours (Figure 3.2c). Between t = +9.88 hours and t = +23.77 hours, the He II, N III, and C III lines almost disappeared while the N II line (5679 Å) became stronger (Figure 3.2b, c)[28]. Between t = +33.94 and t = +71.79 hours, the N II line was weakened, and the Si II (5958/5979 and 6347/6371 Å), O I (7773 Å), and the Al II (6237 Å) lines became stronger (Figure 3.2c, d, e). The N II, Al II, Si II, and Al III (5696.604/5722.730 Å) show multiplets as identified in the HDS spectrum (Figure 3.3; §3.4.3).

We extracted the line luminosities from our spectra; the extinction was corrected for assuming $E(B-V) = 0.51$ (Munari et al., 2021b) and $R_V = 3.1$, and then the flux was converted to the luminosity scale, adopting the Gaia distance (§3.3). The line luminosities at different epochs are summarized in Table 3.2.

The N III and He II lines are rarely found in the early spectra of novae showing the rapid rise (§1.5, chapter 2). Indeed, our spectrum may be a less extreme version of the initial spectrum taken for the recurrent nova T Pyx in 2011 (Arai et al., 2015) at 4.4 hours since the discovery; it showed not only He II and N III lines but also C IV and N IV lines. It is likely that these high-ionization lines are strong only in the short time scale just after the nova eruption; such very early-phase spectra are largely missing in

[27] We note that Fe II lines are seen on its optical maximum (Shore et al., 2021b; Munari et al., 2021a), probably following the temperature decrease.

[28] From the HDS spectrum (§3.4.3.1), we consider that the complex between 4600 Å and 4700 Å observed at t = +23.77, +33.94, +71.79, and +81.90 hours (Figure 3.2b) can be explained by other lines, such as N II (4631/4643 Å) or Al II (4663Å).

the literature[29].

3.4.3 Line Identifications with the HDS Spectrum

The HDS spectrum, with its high resolution and signal-to-noise ratio, allows to separately detect each component of some multiplets. The spectrum thus helps robust identifications of lines when several possibilities are not resolved by the low-resolution data. In this section, we provide line identifications using the HDS spectrum.

3.4.3.1 4600 Å – 4700 Å

The local maxima between 4600 and 4650 Å in the HDS spectrum are consistent with the N II sextuplet (4601.478/4607.153/4613.868/4621.393/4630.539/4643.086 Å; Figure 3.3a); on $t = +53.53$ h, the N III (4638 Å) and C III (4650 Å) lines have already weakened. The Al II singlet (4663.046 Å) is also detected, corroborating our identification of the Al II (6237 Å) line (§3.4.2, 3.4.3.3).

3.4.3.2 5660 Å – 5730 Å

We detected four of the N II sextuplet (with the components at 5666.629/5679.558/5686.213/5710.766 Å detected; those at 5676.017/5730.656 Å non-detected), as well as the Al III doublet (5696.604/5722.730 Å) in the HDS spectrum (Figure 3.3b). The presence of the partner (Al III 5722.730 Å) and the consistency in the relative line strengths (§3.5) justify the identification of the line around 5697 Å in the HDS spectrum ($t = +53.53$ hours) as Al III (5696.604 Å) rather than the C III singlet (5695.916 Å). On the other hand, the component there on $t = +9.88$ hours, as seen in the low-resolution KOOLS-IFU spectrum, is more likely C III rather than Al III (Figure 3.2c; §3.5).

3.4.3.3 6200 Å – 6400 Å

The line frequently refereed to as 'Al II 6237 Å' (Williams, 1992) is actually a triplet (6226.207/6231.7/6243.2 Å; more strictly, it is a sextuplet while some of them are not resolved even in the high-dispersion spectrum). While the triplet is seen as a single line in the KOOLS-IFU spectra ('Al II 6237 Å'; Figure 3.2), it is resolved into the fine structure in the high-resolution HDS spectrum (Figure 3.3c), showing clearer detection of the 6231.7 and 6243.2 Å components. The wavelengths and relative line strengths (including non-detection of the 6226.207 Å component) are consistent with the atomic data of the triplet, which justifies our identification.

[29] Like Gaia22alz (§1.5), extremely slow novae may provides another channel, however, such systems are really rare among novae, and it may well be unwise to think we could understand novae by observing only this population.

3.4.4 Evolution of the Line Profiles

The Hβ and the He I (7065 Å) lines show the P Cygni profile (Figures 3.2 and 3.4), similar to most of the lines that novae typically show around their maxima. The velocity of the blue-shifted absorption minimum of the Hβ line shifts redward from $-1.6(1)\times10^3$ km s^{-1} on $t = +9.88$ hours to $-1.3(7)\times10^3$ km s^{-1} on $t = +81.90$ hours. Similarly, the He I (7065 Å) line seen in the VPH-red spectra shows a decreasing velocity from $-1.6(6)\times10^3$ km s^{-1} on $t = +9.88$ hours to $-1.3(3)\times10^3$ km s^{-1} on $t = +81.90$ hours. Such decreases in the velocities of the absorption components are also found in the Hα and He I (4471 Å) lines. While the velocity measured here using the KOOLS-IFU spectra involves an error of several percent as seen in the comparison between the original HDS spectrum and the one for which the resolution is decreased to the level of the KOOLS-IFU spectra (Figure 3.4a), the deceleration trend is robustly seen beyond the error level.

The deceleration seen in the absorption velocities indicates a homogeneously expanding, ejecta-like outflow, rather than (quasi-)steady wind-like outflow, for the site of the spectral formation in the very early phase (e.g., Aydi et al., 2020). In the ejecta-like outflow, the velocity is usually faster at outer regions (e.g., the Hubble flow). The photosphere is expected to recede in the mass coordinate while it expands outward in radius (Figure 2.1); this behavior could lead to the continuous decrease both in the velocity and temperature, as a general expectation. In contrast, in case of the steady-state wind-like outflow, the velocity and density profiles do not necessarily evolve quickly.

3.5 Analyses of the Line Luminosities

3.5.1 Method

To diagnose the physical conditions responsible for the spectral line formation, we perform crude analyses of the line strengths under the one-zone approximation. The method of the analyses here is briefly described below (for detail, see Appendix A). There are four input parameters; the temperature (T), the gas density (ρ), the composition, and the volume V. For each element, the ionization fractions and level populations are determined by assuming the Local-Thermodynamic Equilibrium (LTE) condition[30], which are then used to compute the line emissivities, through spontaneous emission and recombination. The line luminosities are obtained by multiplying the line emissivities by V.

In addition to the line luminosities, we also estimate the optical depth of the system to the electron scattering;

$$\tau_{\rm e} = n_{\rm e}\sigma_{\rm e}R, \tag{24}$$

[30]This can be justified since the photospheric emission dominates the optical radiation even though the material outside the photosphere produces strong emission lines.

with

$$V = \frac{4\pi}{3} R^3, \tag{25}$$

where n_e is the electron number density, σ_e is the Thomson cross section, and R is the radius. In order to reduce the number of unknown parameters, we further replace the radius and volume of the system with the velocity and time since the outburst (which are both observables), assuming homologous expansion for the dynamics;

$$R = v t_{ej}, \tag{26}$$

with $v = 2000$ km s^{-1} and $t_{ej} = 1$, 2, and 4 days for $t = +9.88$, $+33.94$, and $+81.90$ hours. The other three parameters (ρ, T, and the composition) are allowed to vary. Note that these three parameters are determined by the line strength ratios through the local conditions, and do not depend on the assumed expansion dynamics. Only the conversion from the density to the mass is affected by the size and the volume of the system.

3.5.2 Line Strength Diagnostics

The results of our calculations are compared with the observations in Figure 3.5. Each solid line shows the constraint on a combination of (T, ρ) through the observed luminosity of each line, i.e., the model provides the correct luminosity if T and ρ are on the line. The exercise is done for the data at three epochs (+9.88, +33.94, and +81.90 hours, from top to bottom in Figure 3.5). The left panels show the result adopting the solar abundance (Cox, 2000), while the right panels show the model results adopting the enhancement of nitrogen and aluminum by a factor of 10 and 40 relative to the solar abundance.

On the same plots, we also show the constraint from the non-detection of some lines. The dashed lines show combinations of (T, ρ) that predict line luminosities of 10^{32} erg s^{-1} for some emission lines that are not detected. The adopted luminosity here is a typical upper limit for the non-detection; the region in the (T, ρ) plane above at least one of these dashed lines is thus regarded as 'forbidden'. In addition to this constraint from the undetected lines, we also use the electron scattering optical depth as another constraint; we regard the region where the optical depth exceeds unity as being 'forbidden', as spectral lines will likely be killed once the system suffers from repeated multiple scatterings. The 'forbidden' region is described by the shaded area in Figure 3.5. Assuming the homologously expanding ejecta, the density is converted to the mass ($M = \rho V$) as shown in the right vertical axes.

Panel (a) shows that the line luminosities of the Hα, Hβ, He I, He II, and C III are all explained by $T \sim 22500$ K and $\rho \sim 3 \times 10^{-14}$ g cm^{-3} at $t = +9.88$ hours, with the solar abundance[31]. This condition does not conflict with the non-detection constraints as well. The ejecta mass corresponding to the density here is $\sim 10^{-6}$ $M_\odot$. However, the high luminosities of the nitrogen lines at $t = +9.88$

[31] For the density and temperature considered here, the strength of C III 4650 Å is negligibly small as compared to N III 4640 Å.

hours are not explained by the solar abundance composition. Panel (d) shows that these line strengths are roughly explained if the mass fraction of nitrogen is enhanced by a factor of 10 relative to the solar abundance.

Similar comparisons between the observed and the model line luminosities are shown in panels (b) and (c) for $t = +33.94$ and $+81.90$ hours, respectively. On $t = +33.94$ hours, the line luminosities of the Hα, Hβ, He I, O I, and Si II are consistently explained by $T \sim 10000$ K and $\rho \sim 10^{-14}$ g cm^{-3}, assuming the solar abundance. Similarly, $T \sim 10000$ K and $\rho \sim 3 \times 10^{-15}$ g cm^{-3} explain the luminosities on $t = +81.90$ hours. Again, the model under-reproduces the N II luminosity; this is remedied by increasing the nitrogen enhancement by a factor of 10 as shown in panels (e) and (f), as is consistent with the same enhancement adopted for the earlier epoch.

The strong Al II appears in the spectrum on +33.94 hours, and the similar situation with the nitrogen lines is found for the Al II line; the solar abundance does not produce the Al II luminosity as high as observed, in the physical condition required for the other lines. As shown in panel (e), if the mass fraction of aluminum is enhanced by a factor of ~ 40 relative to the solar abundance, the observed luminosity is reproduced. We confirm that the enhancement of nitrogen and aluminum does not introduce inconsistency with the upper limit placed for the non-detected lines. Essentially the same argument applies to the spectrum on +81.90 hours; we need the enhancement of nitrogen and aluminum by a factor of ~ 10 and 40, respectively, while keeping the solar abundance for the other elements (panels c and f).

We find that the density and temperature of the line-forming region both decrease as time goes by. This is most simply explained by the expanding 'ejecta' or 'fireball', on top of the expanding photosphere, rather than the wind-like mass outflow, as is consistent with the line-velocity evolution (§3.4.4). If it is interpreted as the homologously expanding ejecta, the mass of the line-forming region also increases for later epochs. This can be explained by increasing transparency due to the expansion, again consistent with the expanding ejecta picture.

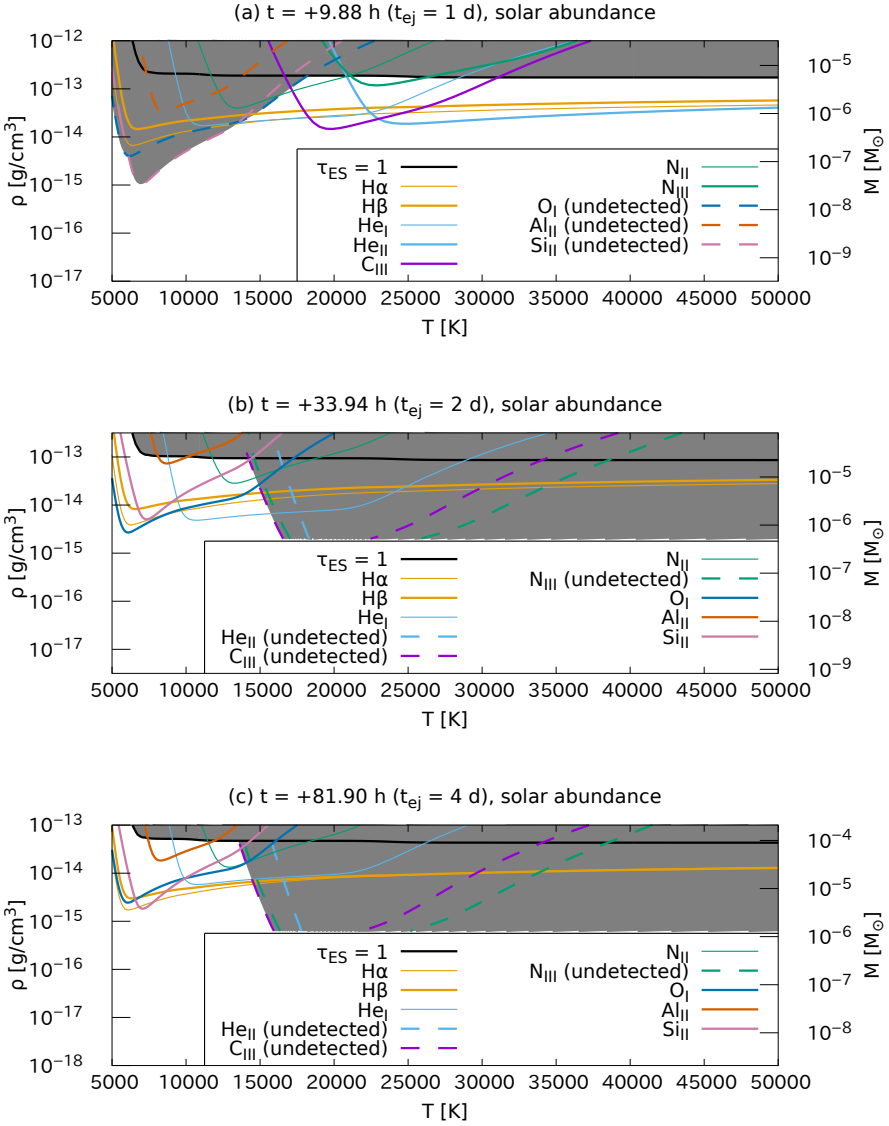

Figure 3.5: Constraints on the conditions of the line-forming region in the (T, ρ) plane for (a,d) t = +9.88, (b,e) t = +33.94, and (c,f) t = +81.90 hours. The observed line luminosities are reproduced by the one-zone model on the colored curves, where different colors are used for different lines; a consistent solution is therefore found for the position of (T, ρ) where all the lines are largely overlapping with each other. For the non-detected lines, we place the limits in the (T, ρ) plane as shown by the colored dashed lines (with different colors for different lines), using the typical sensitivity of 10^{32} erg s^{-1} for the non-detection. The black line in each panel shows the constraint of the electron scattering optical depth being unity, above which the line formation will become ineffective. The shaded area in each panel shows the 'forbidden' region, where either at least one of the non-detection constraints or electron-scattering optical depth constraint is not satisfied. (a,b,c) the solar abundance for all the elements. (*continued on the next page*)

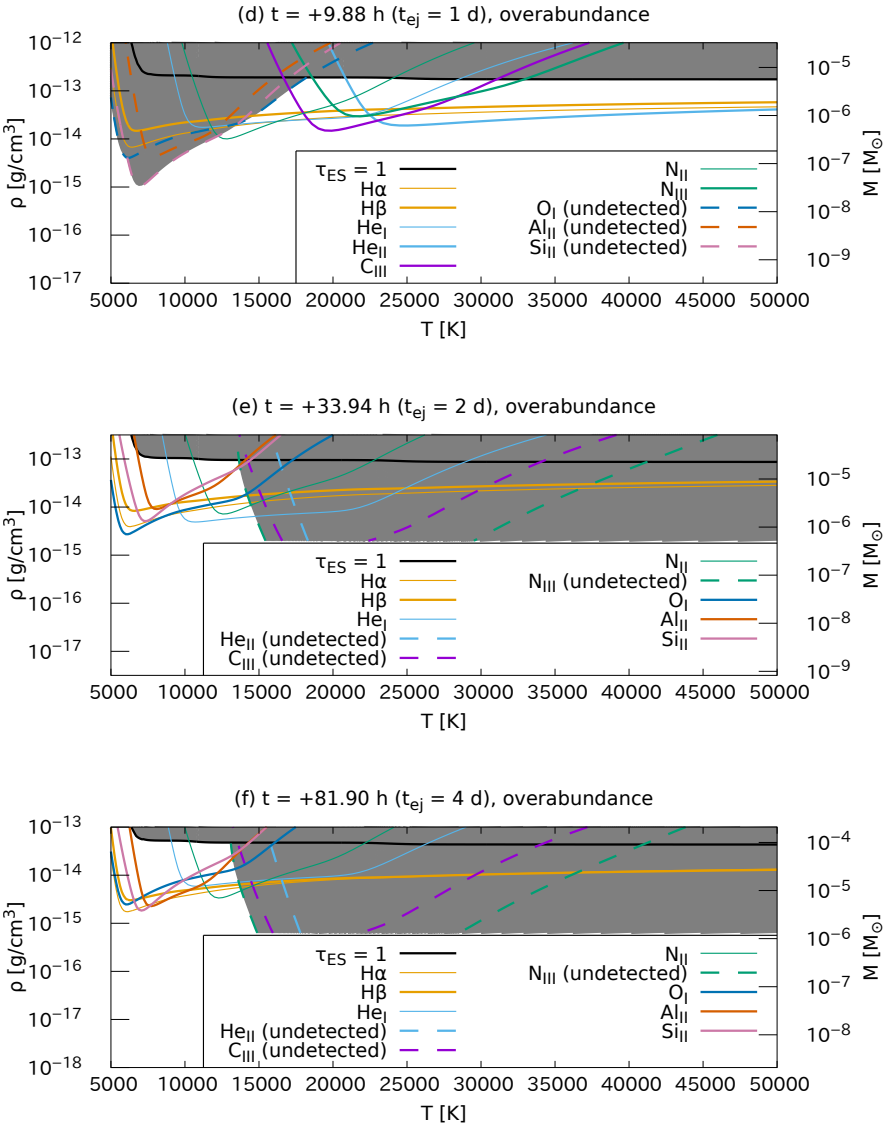

Figure 3.5 (Continued): (d,e,f) same as panels (a,b,c), while adopt the enhanced mass fractions for nitrogen and aluminum, by a factor of 10 and 40 relative to the solar abundance, respectively.

3.6 Discussion

3.6.1 A Low Mass ONeMg WD behind V1405 Cas

We have found the enhancement of the mass fraction of aluminum in V1405 Cas, by a factor of $\sim$ 40 relative to the solar abundance (§3.5.2), based on the detection of the Al II 6237 Å line. From nucleosynthesis models of novae (§1.4), such a large excess of aluminum in a nova indicates an ONeMg WD progenitor rather than a CO WD, because the Ne-Na and Mg-Al cycles work much more efficiently in the ONeMg WD case. Therefore, we conclude that the WD behind V1405 Cas is likely an ONeMg WD, as is consistent with the neon-nova classification reported by Munari & Valisa (2022) based on

its spectra in the decay phase[32]. The low-mass progenitor for V1405 Cas is also consistent with the spectral property; it shows narrower emission lines (cf., §3.4.2) than novae hosting massive WDs like U Sco (Yamanaka et al., 2010).

To our knowledge, V723 Cas is the only previous example of a very slow nova classified as a neon nova. Indeed, the observational properties of V723 Cas show similarities to V1405 Cas. After the maximum light, V723 Cas showed humps with repeated brightening and fading in its light curve, a striking property that is very similar to what is seen in V1405 Cas. The WD mass, $M_{\rm WD}$, is estimated to be below 0.7 $M_\odot$ for V723 Cas from the light curve (Hachisu & Kato, 2015). Therefore V723 Cas had been initially considered as a CO nova (Hachisu & Kato, 2004; Iijima, 2006). However, Iijima (2006) derived the abundance of neon in V723 Cas as $\log(N_{\rm Ne}/N_{\rm H}) = -2.5$ (i.e., Ne/H $\sim$ 26 (Ne/H)$_\odot$), and Takeda et al. (2018) summarized that V723 Cas is the first example of a very slow nova showing a signature of being a neon nova, hosting a WD of only $\sim 0.6\ M_\odot$.

V1405 Cas is the second example of this kind; a very slow nova classified as a neon nova. Such a low mass ONeMg WD is not expected in the standard theory of single-star evolution (§3.2). However, as proposed by Kepler et al. (2016) and Takeda et al. (2018), it may be explained by extensive mass loss through binary evolution, a late violent thermal pulse, or a C-shell flash. In these cases, the WD has to lose $\sim 0.5\ M_\odot$ since the formation, and whether such an evolution is possible has not been clarified. Further study to identify possible evolutionary channel(s) for the formation of a low-mass ONeMg WD is required, which hopefully will deepen our understanding of the formation and evolution of WDs.

3.6.2 Aluminum overabundance and neon novae

As argued in §1.4 and §3.6.1, the aluminum overabundance is expected for neon novae according to nucleosynthesis calculations. There is indeed a hint of this signature seen in previous observations of novae in the decline phases. For example, V838 Her, which is one of the fastest neon novae, has aluminum abundance Al/H $\sim$ 23 (Al/H)$_\odot$ as was derived based on ultraviolet observations (Schwarz et al., 2007). Likewise, based on UV observations, the aluminum excesses have been derived for very fast neon novae LMC 1990#1 (Al/H $\sim$ 292 (Al/H)$_\odot$; Vanlandingham et al., 1999), V382 Vel (Al/H $\sim$ 20.6 (Al/H)$_\odot$; Shore et al., 2003), V351 Pup (Al/H $\sim$ 140 (Al/H)$_\odot$; Saizar et al., 1996), and V693 CrA (Al/H $\sim$ 64 (Al/H)$_\odot$; Vanlandingham et al., 1997), and fast neon novae V1974 Cyg (Al/H = 8.2 (Al/H)$_\odot$; Austin et al., 1996) and QU Vul (Al/H $\sim$ 39-376 (Al/H)$_\odot$; Saizar et al., 1992; Andrea et al., 1994; Schwarz, 2002). This is further added by the aluminum excess derived for neon novae based on NIR observations; an example is the very fast nova V1500 Cyg (Al/H $\geq$ 22 (Al/H)$_\odot$; Woodward et al., 1995; Boiarchuk et al., 1977). These examples hint the possible relation between the aluminum excess and neon novae (i.e., ONeMg WD progenitors), as expected from the nucleosynthesis point of view. However, we emphasize

[32]We indeed had reached this conclusion before Munari & Valisa (2022) classified V1405 Cas as a neon nova (e.g., https://sites.google.com/view/supervirtual2022/home).

that not all novae showing aluminum excesses are neon novae; Orio et al. (2020) reported $\mathrm{Al/Al}_{\odot} = 172^{+153}_{-63} - 0.0^{+1.0}$ from the *Chandra* observation of the symbiotic recurrent CO nova V3890 Sgr.

Indeed, it is further complicated by the case of V723 Cas – while it was reported as the first case of the 'very slow neon nova' (see above), the aluminum abundance is not enhanced; the photoionization model (Takeda et al., 2018) for the data taken by Keck-OSIRIS (Lyke & Campbell, 2009) indicates $\mathrm{Al/H} = 1.3\ (\mathrm{Al/H})_{\odot}$, unlike the case for V1405 Cas. Therefore, the relation between the aluminum enhancement and the ONeMg WD progenitor requires further investigation and clarification.

3.6.3 Al II λ6237 as the earliest indicator for a neon nova

Neon novae are rare. This is especially the case for slow *and* neon novae. As such, it is useful to identify neon nova candidates as early as possible before the definitive classification is given through the late-time neon lines, so that intensive follow-up observations can be coordinated from the early phase.

The present work suggests that Al II λ6237 can be a useful predictor that can be used as the earliest footprint to identify a neon nova 'candidate' (with the caveat that the relation between the aluminum enhancement and the neon nova is yet to be established; §3.6.2). As shown in the present work, V1405 Cas shows the rapid decrease in the temperature in the initial rising phase. While the spectral observations in such short initial brightening phases are still lacking for novae (except for V1405 Cas and T Pyx), we expect that it is a general behavior of novae. In the subsequent pre-maximum halt phase, the high density of the emitting region (as shown in the present work) allows sufficiently strong Al II λ6237, while another potentially strong line, Al II λ7049, is easily masked by He I (7065 Å) line; it is thus expected that Al II λ6237 first emerges as the earliest prophet for a neon nova in the high-temperature condition (i.e., He/N-type), which is later added by Al II λ7049 once the temperature decreases sufficiently so that the He lines disappear (i.e., Fe II-type)[33].

This is especially useful for slow novae. Fast novae are generally believed to have a low density in the ejecta (due to the small ejecta mass and the high expansion velocity), and thus the phase where Al II λ6237 emerges is likely very limited, or even lacking. On the other hand, slow novae likely have high-density ejecta especially in the earliest phase, and thus detection of Al II λ6237, if one is indeed a neon nova, is expected if sufficiently early-phase spectral observations are conducted. This has been demonstrated by the present work; it helps to organize further follow-up observations not to miss an opportunity to form intensive data set for these rare but important events.

[33]Indeed, Al II λ7049 was identified in the Fe II-type spectrum of fast neon nova V2264 Oph (Williams et al., 1994). In the subsequent He/N-type spectrum with [O I] (their Fig. 7), Al II $\lambda\lambda$ 3901, 4863, and 10090 were identified, and potential Al II λ 6237, which they did not identify, is seen.

3.7 Concluding Remarks

We have presented our spectroscopic observations of the very slow nova V1405 Cas in six epochs between t = +9.88 hours and t = +81.90 hours after its discovery, covering between the end of the initial brightening and the earliest stage of the pre-maximum halt. The key findings are summarized as follows;

- V1405 Cas initially showed high-ionization lines (e.g., N III), which are rapidly replaced by lower-ionization lines (e.g., N II).
- We see a rapid decrease in the density and temperature, as well as an increase in the emitting mass. These are consistent with the idea that the initial phase of a nova is well described as an expanding fireball on top of an expanding photosphere.
- The Al II line (6237 Å) is detected on t = +23.77, +33.94, +53.53, +71.79, and +81.90 hours. We have estimated that aluminum is overproduced in the nova ejecta, by a factor of $\sim$ 40 relative to the solar abundance. Similarly, nitrogen is enhanced by a factor of $\sim$ 10.

We have concluded that V1405 Cas likely hosts a low-mass ONeMg WD, strengthening its classification as a very slow *and* neon nova; this is the second example of this kind.

- V1405 Cas is similar to V723 Cas in characteristic observational features; a very slow light curve with humps seen after the maximum light, as well as the neon nova classification based on coronal neon lines in the decline phase. We suggest that the aluminum overabundance in V1405 Cas supports its origin as a low-mass ONeMg WD.
- Motivated by the results of reaction-network model calculations that generally predict a huge enhancement of aluminum abundance in a neon nova as compared to a CO nova, together with the aluminum enhancement seen in V1405 Cas, we have investigated a possible relation between the aluminum enhancement and their classification. While the survey is neither complete nor unbiased, there is a hint that fast novae showing aluminum excesses tend to be neon novae, indicating that this relation is roughly the case. However, the exceptions are also found (i.e., CO novae with the aluminum enhancement, as well as neon novae with the aluminum non-enhancement; the latter is the case for V723 Cas), and thus further investigation is required before establishing the relation.

Further theoretical studies are necessary to investigate the properties of these very slow novae; neon novae having such a low-mass ONeMg WD progenitor have not been investigated by model calculations, because such systems have not been in attention. Given the proximity of V1405 Cas that allows further monitoring observations even toward its staying back to the quiescent state, further follow-up observations are encouraged to deepen our understanding of neon novae and their contribution to the Galactic chemical evolution (cf., §1.4). In addition, with Al II λ6237 (and later λ7049) as the earliest indicator for a neon

nova, we hope to substantially expand the sample of neon novae with intensive observational data already from the infant phase.

Given the proximity of V1405 Cas that allows further monitoring observations even toward its staying back to the quiescent state, further follow-up observations are encouraged to deepen our understanding of neon novae and their contribution to the Galactic chemical evolution. In addition, with Al II λ6237 (and later λ7049) as the earliest indicator for a neon nova, we hope to substantially expand the sample of neon novae with intensive observational data already from the infant phase.

3.8 Acknowledgements for the contents of Chapter 3

This study makes use of data obtained by the 3.8-m Seimei telescope through the programs, 21A-N-CT06 in the open-use of the observing time provided by NAOJ and 21A-K-0017 in the Kyoto University time. The Seimei telescope at the Okayama Observatory is jointly operated by Kyoto University and the Astronomical Observatory of Japan (NAOJ), with assistance provided by the Optical and Near-Infrared Astronomy Inter-University Cooperation Program. This research is based in part on data collected at the Subaru Telescope, which is operated by the National Astronomical Observatory of Japan. We are honored and grateful for the opportunity of observing the Universe from Maunakea, which has the cultural, historical and natural significance in Hawaii. We acknowledge the AAVSO International Database contributed by observers worldwide. This work has made use of data from the European Space Agency (ESA) mission *Gaia* (https://www.cosmos.esa.int/gaia), processed by the *Gaia* Data Processing and Analysis Consortium (DPAC, https://www.cosmos.esa.int/web/gaia/dpac/consortium). Funding for the DPAC has been provided by national institutions, in particular the institutions participating in the *Gaia* Multilateral Agreement. This work is supported by JST SPRING grant JPMJSP2110 (Kenta Taguchi) and by JSPS KAKENHI grants JP18H05223, JP20H04737, JP20H00174 (Keiichi Maeda), JP22K03676 (Masayuki Yamanaka), JP20K14521, JP18H05439 (Keisuke Isogai), 21J22351 (Yusuke Tampo), and JP21K03616 (Taichi Kato).

Chapter 4

Summary and Future Prospects

Thanks to the recent developments in transient surveys, observing the earliest stages of novae in detail becomes feasible once a dedicated follow-up program is established. We have been constructing such a rapid follow-up program of novae, by making the best use of the rapid ToO capability of the Seimei telescope. As one of the highlights from the program, we have managed to take a spectrum of V1405 Cas during its initial brightening phase that confirms the theory of the initial brightening (§1.5, Figure 2.1). The theory has long been accepted widely, but there have indeed been few direct observational evidences; the hot photosphere during the initial brightening phase, as a key prediction from the theory, has been directly tested only by Arai et al. (2015). Our observation, reveling the initial high temperature of the expanding photoshpere, has added a new example that confirms the standard theory of nova ejecta dynamics (see also König et al., 2022, for eROSITA detection for YZ Ret).

Our key findings in the V1405 Cas spectra are (1) highly-ionized lines of He II and N III only during the initial brightening stage, (2) decelerating trends in the velocities of absorption components of Balmer and He I lines, and (3) aluminum overabundance. Our framework, created for relating the density, temperature, and chemical abundance to the emission line strengths under the one-zone approximation, enables us to qualitatively confirm not only (1) but also (3). (1) is the direct evidence of the initial high temperature. (2) can be naturally explained by the expanding photosphere. (3) is, as we have discussed in the main text, a prophet for a neon nova, which confirms, with the very slow light curve, a very low-mass white dwarf behind V1405 Cas.

To further deepen our understanding of the infant stages of novae, observing the time evolution of novae in such stages is indispensable. Therefore, we set the next goal of our program to take optical spectra twice or more during its initial brightening; such observation has not been realized either by Arai et al. (2015) (T Pyx in 2011) or by the present observations (V1405 Cas in 2021) due to the bad visibility. Note that Quimby et al. (2021) reported a detailed light curve of V1674 Her, one of the fastest novae ever observed, in its very infant stage by their 2-min cadence survey. Their detection of the

plateau in the light curve ~ 8 magnitudes below the peak is record-breaking. However, the construction of the initial light curve of V1674 Her was done only after the discovery of V1674 Her, i.e., it was not a real-time reconstruction. If such short-time cadence surveys, especially Tomo-e gozen (Sako et al., 2018) at the Kiso observatory whose latitude and longitude are close to those of Okayama, evolve to alert the nova detections in real-time, our goal will have a better chance to be realized.

I also hope to further explore such early spectra of novae for diagnosing the state of the binary system just before novae start. Only from sufficiently early nova spectra, the CSM having already existed before the nova starts is expected to be observed (Figure 2.1). Since the nova photosphere is as luminous as the Eddington luminosity (§1.5), we expect the photospheric emission to illuminate the CSM so effectively that we may observe emission lines from the CSM by spectroscopy. Some spectra reported so far, e.g., those of RS Oph (Figures 2.2 and 2.3), may indeed reflect such a configuration. Non-LTE spectrum modeling is desired to diagnose the structure and temperature in the CSM. Another fruit of non-LTE spectrum modeling is more precise abundance and temperature determination in nova ejecta while it is not expected to change the result of aluminum overabundance in V1405 Cas (§A.6).

In addition, we can investigate properties of nova ejecta from emission lines in nova spectra. The ejecta include not only material from the secondary but also those from the WD and those burnt during the nova. Therefore, to determine whether a WD in a nova is a CO WD (in a CO nova) or an ONeMg WD (in a neon nova), nova spectra provide key information (§1.4). The neon nova is defined as a nova showing neon forbidden lines in the nebular spectra. However, for very slow neon novae, the existence of which has been confirmed by the present work, it takes a long time for the photosphere to shrink, starting to show the neon lines. As we have demonstrated for V1405 Cas (§3), aluminum lines can be a great prophet to uncover the nature of such novae within the first days. As a future prospect, this signature may enable us not to miss such rare events already soon after the discovery of novae, without waiting for a long time until they enter the nebular stage.

The isotope ratios in novae are also of interest. Tajitsu et al. (2015) distinguishes beta-unstable ^{7}Be II from stable ^{9}Be II to prove lithium production in a classical nova. As a future perspective related to the present work on V1405 Cas, not a CO nova but a neon nova with aluminum excess, the aluminum isotope ratio ^{26}Al/^{27}Al should be of interest. ^{26}Al is not only the source of the gamma-ray emission line but also an important player in planetary physics (e.g., thermal inversions in atmospheres of hot Jupiters, Gandhi & Madhusudhan, 2019). However, the origin of ^{26} is still uncertain. Several attempts are there to detect ^{26}AlO for astrophysical objects (e.g., Banerjee et al., 2004, for the luminous red nova V4332 Sgr), but have so far only provided upper limits (Bowesman et al., 2021). There is an example of possible AlO detection in an old nova GK Per many years after the nova outburst (Bianchini in Hack et al., 1993). V1405 Cas may show an AlO band that can be split into isotopes by modern observations.

I will continue to work on this program, conducting the time-series optical spectra during the initial

brightening as well as the emission line modeling (to be applicable to RS Oph as an immediate project). Also, I will keep monitoring spectra taken by our program and other groups so as not to miss future very slow neon nova candidates.

Appendix A

Computations of the Line Strengths

We approximate the line luminosity $L_{u\to l}$ and line emissivity $j_{u\to l}$ of a transition from upper level u to lower level l as the sum of the following two components,

$$L_{u\to l} = L^{\rm spon}_{u\to l} + L^{\rm recomb}_{u\to l} \tag{27}$$

$$= (j^{\rm spon}_{u\to l} + L^{\rm recomb}_{u\to l})V \tag{28}$$

$$= j_{u\to l}V, \tag{29}$$

where $L^{\rm spon}_{u\to l}$ (or $j^{\rm spon}_{u\to l}$) is the spontaneous component (§A.4) for given level populations, and $L^{\rm recomb}_{u\to l}$ (or $j^{\rm recomb}_{u\to l}$) is the recombination component §A.5 for given ionization status. Here, V is the volume of the system.

In the present work, we assume the ejecta-like outflow, which is justified by the decrease in the line velocities with time (§3.4.4). V is then related to the typical size of the system R as

$$V = \frac{4\pi}{3}R^3, \tag{30}$$

and R can be expressed as

$$R \sim 2.5\times10^2 R_\odot \left(\frac{v}{2000\ {\rm km\ s^{-1}}}\right)\left(\frac{t_{\rm ej}}{1\ {\rm day}}\right), \tag{31}$$

where v is the velocity of the ejecta and $t_{\rm ej}$ is the time that has passed since the outburst. In this thesis, we adopt $v = 2000$ km s^{-1}. As is in table 3.2, we adopt $t_{\rm ej} = 1$, 2, and 4 days for $t = +9.88$, $+33.94$, and $+81.90$ hours, respectively.

Table A.1: Elements considered in our calculation. The atomic mass is in units of duodecimal of the mass of ^{12}C. The abundance ratios used in the text are also listed.

Atom	Atomic Number	Atomic Mass	$\log_{10}$(Solar abundance)	$\log_{10}$(Excess abundance)
H	1	1.007	12.00	12.00
He	2	4.002	10.99	10.99
C	6	12.011	8.56	8.56
N	7	14.007	8.05	**9.05**
O	8	15.999	8.93	8.93
Ne	10	20.180	8.09	8.09
Na	11	22.990	6.33	6.33
Mg	12	24.305	7.58	7.58
Al	13	26.982	6.47	**8.07**
Si	14	28.086	7.55	7.55
S	16	32.066	7.21	7.21
Ar	18	39.948	6.56	6.56
Ca	20	40.078	6.36	6.36
Fe	26	55.847	7.54	7.54

A.1 Atomic Data

In our calculation, we include elements listed in Table A.1 and make use of the atomic database of *CMFGEN*[34] (Hillier & Miller, 1998; Hillier, 1990). The number of levels we used for this calculation is listed in Table A.3. For example, we used 36 levels of H I from $n = 1$ to 30 (for $n = 2$, 3, and 4, we split into different l-s).

A.2 Level Population

Here, the level populations are calculated in the LTE assumption. For example, the number density of level l of Al II ion is

$$\frac{n_l}{n(\mathrm{Al\ II})} = \frac{g_l}{Z(\mathrm{Al\ II})} \exp\left(-\frac{E_l}{k_\mathrm{B}T}\right), \tag{32}$$

where g_l is the degeneracy of l, E_l is the excitation energy of l from the ground state of Al II, and k_B is the Stefan-Boltzmann constant. Here,

$$Z(\mathrm{Al\ II}) = \sum_l g_l \exp\left(-\frac{E_l}{k_\mathrm{B}T}\right), \tag{33}$$

[34] https://kookaburra.phyast.pitt.edu/hillier/web/CMFGEN.htm

is the partition function[35] of Al II. The populations between levels i and j with one different electron number follow the **Saha equation**,

$$\frac{n_j n_\mathrm{e}}{n_i} = \frac{2g_j}{g_i \lambda_\mathrm{Te}^3} \exp\left(-\frac{h\nu_{ij}}{k_\mathrm{B}T}\right). \tag{34}$$

Here, $h\nu_{ij}$ is the energy required for the transition from i to j which is identical to the ionization energy if both i and j are ground states, and

$$\lambda_\mathrm{Te} = \frac{h}{\sqrt{2\pi m_\mathrm{e} k_\mathrm{B} T}}, \tag{35}$$

is the **thermal de-Broglie wavelength** of free electrons.

A.3 Solving Level Population

First, for the given mass density ρ and abundance ratio, we can derive the number densities of all elements (n(H), n(He), $\cdots$) by using

$$\rho = m_\mathrm{H} n(\mathrm{H}) + m_\mathrm{He} n(\mathrm{He}) + \cdots. \tag{36}$$

Then, we solve n_e and level populations by an iterative procedure. In usual gases, free electrons are from hydrogen. Therefore, we can get an approximate value of n_e by considering the pure hydrogen gas. If we denote the ionization degree of hydrogen α and ignore the excited states of H I,

$$\frac{\alpha^2}{1-\alpha} n(\mathrm{H}) = \frac{1}{\lambda_\mathrm{Te}^3} \exp\left(-\frac{\chi}{k_\mathrm{B}T}\right). \tag{37}$$

Here, $\chi = 13.6$ eV is the ionization energy of H I. We calculate α for a given n(H) and T to obtain an approximate value of $n_\mathrm{e} = \alpha n(\mathrm{H})$. Starting with this n_e, we iterate by (i) calculating the level populations of each element (e.g., aluminum) by LTE relations (32) and (34) with

$$n(\mathrm{Al}) = n(\mathrm{Al\ I}) + n(\mathrm{Al\ II}) + n(\mathrm{Al\ III}) + \cdots, \tag{38}$$

and (ii) updating n_e by charge neutrality

$$n_\mathrm{e} = -n(\mathrm{H}^-) + n(\mathrm{H\ II}) + n(\mathrm{He\ II}) + 2n(\mathrm{He\ III}) + \cdots, \tag{39}$$

until n_e converges.

[35] Note that we have to cut off the number of levels included in the calculation of the partition function to prevent divergence (see also Table A.3). For example, the degeneracy g_n and energy E_n of the hydrogen atom in principal quantum number n is proportional to n^2 and $-1/n^2$, respectively. Therefore, $n^2 \exp(-E_n/(k_\mathrm{B}T))$ must diverge. Indeed, we do not consider such divergence to be the case; this paradox is from the deviation from the LTE assumption when n gets large.

A.4 Spontaneous Component

The spontaneous component is expressed as

$$j^{\rm spon}_{u\to l} = \frac{h\nu_{ul}}{4\pi} n_u A_{ul}, \tag{40}$$

where ν_{ul} is the line frequency, n_u is the number density of the upper level, A_{ul} is Einstein's A coefficient, and V is the volume of the system (see below). It should be the very emissivity in the LTE limit without background radiation (here we ignored induced emission).

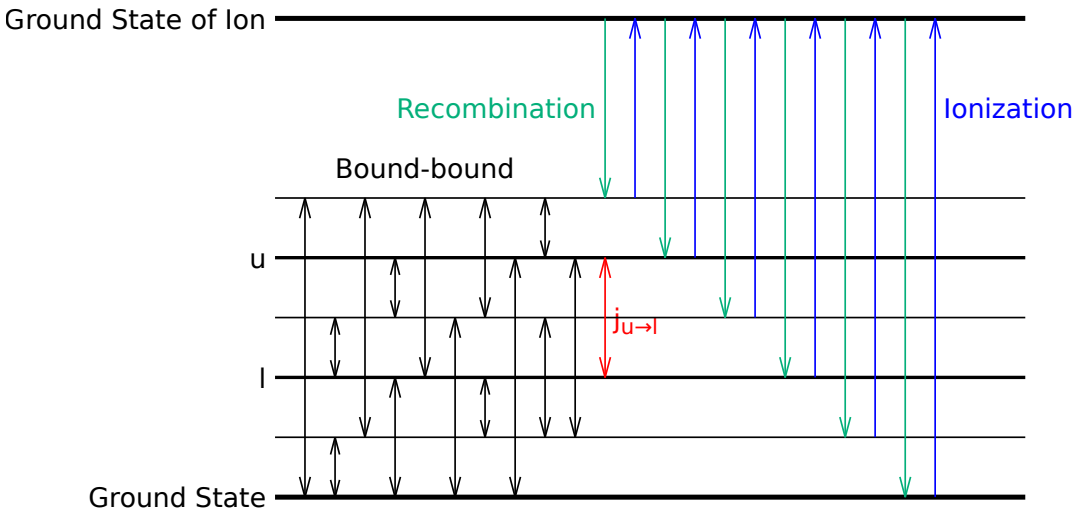

Figure A.1: A conceptual diagram of LTE condition (**detailed balance**). Each bound-bound excitation balances with its reverse, de-excitation (black and red arrows). So does bound-free ionization (blue arrow) with free-bound recombination (green arrow).

A.5 Recombination Component

If T is high (e.g., $\gtrsim$ 10000 K for He I 7065 Å, Figure A.8), n_u-s of excited levels become small because of ionization. Then, the spontaneous emission should become inefficient. Or, the LTE assumption for these excited levels may even be invalid; alternatively, it may be more precise to have a picture that, for He I lines as an example, He II ions in the ground state[36] recombine to the excited state of He I, which emits He I lines when it cascades to the ground state of He I. To represent this situation, we assume that the populations in ground states of He I and He II balance each other following the Saha equation and that the ionization from the ground state of He I to the ground state of He II balances

[36] For simplicity, we consider recombinations from only the ground state.

with recombination from the ground state of He II to all the states of H I. In other words, we simplify the non-LTE situation.

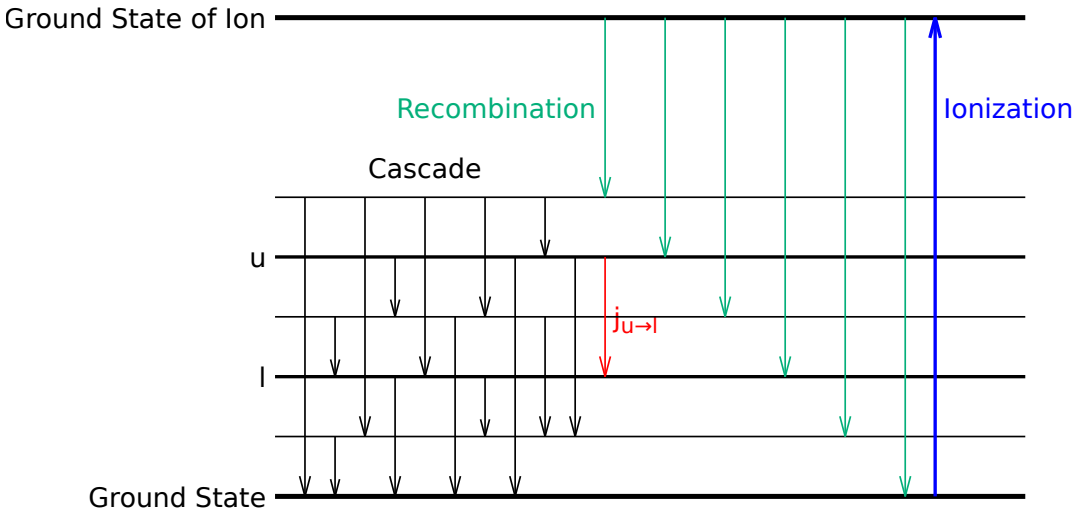

Figure A.2: A conceptual diagram of LTE condition (**detailed balance**). For He I line as an example, ionization from the ground state of He I to the ground state of the 'upper' ion He II (blue arrow) balance to the sum of recombinations from the ground state of He II to all the states of He I (green arrows). The balance is because we assume it immediately cascades to the ground state (black and red arrows) once it recombines.

Then, the recombination emissivity can be evaluated as

$$j^{\rm recomb}_{u\to l} = \frac{h\nu_{ul}}{4\pi} n_{\rm ion} n_{\rm e} \alpha^{\rm (total)}_{{\rm ion}\to u}(T) P^{\rm (direct)}_{u\to l}, \tag{41}$$

where $n_{\rm ion}$ is the number density of the 'upper' ion (e.g., He II for considering He I emission lines), $n_{\rm e}$ is the number density of electrons, $\alpha^{\rm (total)}_{{\rm ion}\to u}(T)$ is the 'total' recombination coefficient (defined later) from upper ion to level u, and $P^{\rm (direct)}_{u\to l}$ is the transition probability from level u to level l 'directly' (i.e., without transitioning to intermediate states before going down to level l).

$P^{\rm (direct)}_{u\to l}$ is determined by the Einstein's A coefficients as follows;

$$P^{\rm (direct)}_{u\to l} = \frac{A_{ul}}{\sum_{l'<u} A_{ul'}}, \tag{42}$$

where $\sum_{l'<u}$ means that it is summed over all the levels l' whose energy eigenvalues are lower than that of level u (Figure A.3).

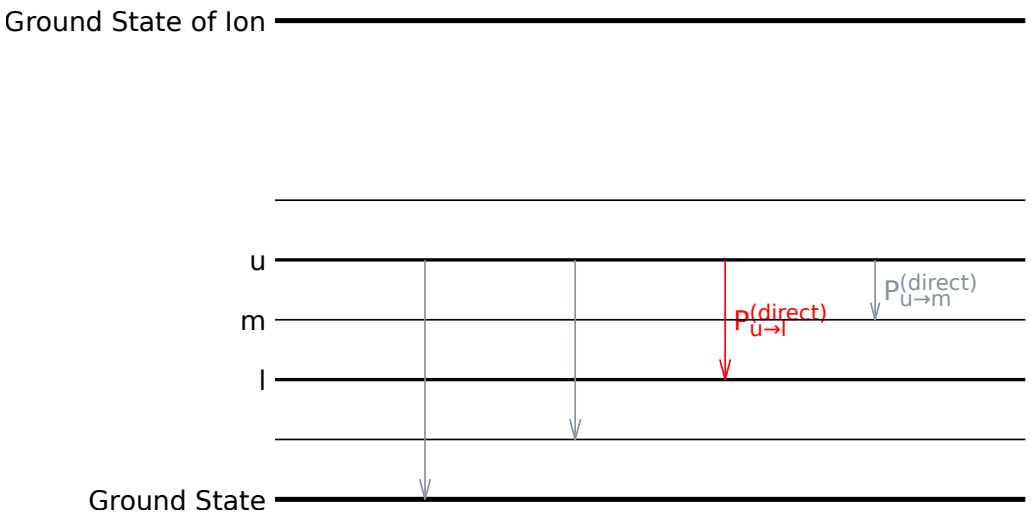

Figure A.3: Explanatory diagram for equation (42). From level u, there are several choices for the 'direct' bound-bound transition. $P^{(\mathrm{direct})}_{u\to l}$ is the probability of the choice to level l.

The 'total' recombination coefficient $\alpha^{(\mathrm{total})}_{\mathrm{ion}\to u}(T)$ is defined as

$$\alpha^{(\mathrm{total})}_{\mathrm{ion}\to u}(T) = \alpha^{(\mathrm{direct})}_{\mathrm{ion}\to u}(T) + \sum_{u'>u} \alpha^{(\mathrm{direct})}_{\mathrm{ion}\to u'}(T) P^{(\mathrm{total})}_{u'\to u}, \tag{43}$$

(Figure A.4), where

$$P^{(\mathrm{total})}_{u\to l} = P^{(\mathrm{direct})}_{u\to l} + \sum_{l<m<u} P^{(\mathrm{direct})}_{u\to m} P^{(\mathrm{total})}_{m\to l} \tag{44}$$

is the 'total' probability that an ion at level u transitions to level l through any combinations of different transitions (Figure A.5), and $\alpha^{(\mathrm{direct})}_{\mathrm{ion}\to u}(T)$ is the 'direct' recombination coefficients to level u.

The recombination coefficients can be evaluated by the photoionization cross section $\sigma_{u\to\mathrm{ion}}(\nu)$ via

$$\alpha^{(\mathrm{direct})}_{\mathrm{ion}\to u}(T) = \frac{n_u}{n_{\mathrm{ion}} n_{\mathrm{e}}} \int_{\nu_{\mathrm{th}}}^{+\infty} \frac{4\pi \tilde{B}_\nu(T)}{h\nu} \sigma_{u\to\mathrm{ion}}(\nu)\,\mathrm{d}\nu. \tag{45}$$

Here,

$$\tilde{B}_\nu(T) = \frac{2h\nu^3}{c^2} \exp\left(-\frac{h\nu}{k_{\mathrm{B}}T}\right), \tag{46}$$

is a 'pseudo' Planckian function[37].

[37] In the complete thermal equilibrium limit, the number of photoionizations by photons whose frequencies are between ν and $\nu + \mathrm{d}\nu$ in unit time and volume is,

$$n_u \frac{4\pi B_\nu(T)\,\mathrm{d}\nu}{h\nu} \sigma_{u\to\mathrm{ion}}(\nu). \tag{47}$$

One may consider its integral over ν balances to the recombination ($= n_{\mathrm{ion}} n_{\mathrm{e}} \alpha$) and wonder not $B_\nu(T)$ but $\tilde{B}_\nu(T)$ is used in (45). This is because we ignored the effect of 'induced' recombination.

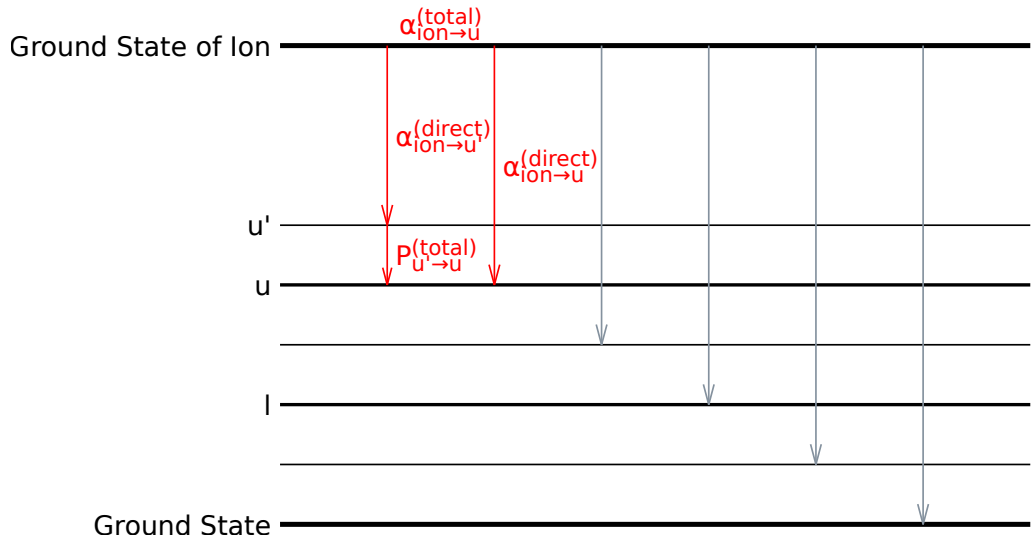

Figure A.4: Explanatory diagram for equation (43). $\alpha^{(\mathrm{total})}_{\mathrm{ion}\to u}$ is the 'total' recombination rate from the ion to level u. It does not include only the 'direct' recombination $\alpha^{(\mathrm{direct})}_{\mathrm{ion}\to u}$ but also 'direct' recombinations to upper levels $u'(>u)$ weighted by the 'total' transition probability $P^{(\mathrm{total})}_{u'\to u}$ from these u'-s to level u.

A.6 The Ratio of the Two Emissivities

From (40) and (41),

$$\frac{j^{\mathrm{recomb}}_{u\to l}}{j^{\mathrm{spon}}_{u\to l}} = \frac{n_{\mathrm{ion}} n_{\mathrm{e}}}{n_u} \frac{\alpha^{(\mathrm{total})}_{\mathrm{ion}\to u}(T) P^{(\mathrm{direct})}_{u\to l}}{A_{ul}}. \tag{52}$$

Therefore, using the Saha equation (34), it is obvious that this ratio depends only on T (i.e., it does not depend on ρ). Figures A.6 to A.13 show the ratios for some lines. They show the ratios are monotonically increasing functions of T and large for Hα, Hβ, N II, O I, and especially He I (i.e., for other lines the line luminosity should be reproduced by the spontaneous component).

The number of recombinations of electrons whose velocities are between v_{e} and $v_{\mathrm{e}} + \mathrm{d}v_{\mathrm{e}}$ in unit time and volume is,

$$n_{\mathrm{ion}} \frac{\mathrm{d}n_{\mathrm{e}}}{\mathrm{d}v_{\mathrm{e}}} \mathrm{d}v_{\mathrm{e}}\, v_{\mathrm{e}} \sigma_{\mathrm{ion}\to u}(v_{\mathrm{e}}). \tag{48}$$

Here, $\sigma_{\mathrm{ion}\to u}(v_{\mathrm{e}})$ is the recombination cross-section, and $\mathrm{d}n_{\mathrm{e}}/\mathrm{d}v_{\mathrm{e}}$ is the electron density in unit velocity. If it is in thermal equilibrium,

$$\frac{\mathrm{d}n_{\mathrm{e}}}{\mathrm{d}v_{\mathrm{e}}}(T) = 4\pi n_{\mathrm{e}} v_{\mathrm{e}}^2 \left(\frac{m_{\mathrm{e}}}{2\pi k_{\mathrm{B}} T}\right)^{3/2} \exp\left(-\frac{m_{\mathrm{e}} v_{\mathrm{e}}^2}{2k_{\mathrm{B}} T}\right). \tag{49}$$

In thermal equilibrium, (47) and (48) balance, and therefore,

$$\sigma_{\mathrm{ion}\to u}(v_{\mathrm{e}}; T) = \frac{g_u h}{2 g_{\mathrm{ion}} m_{\mathrm{e}}^2 v_{\mathrm{e}}^2} \frac{\sigma_{u\to \mathrm{ion}}(\nu)}{\nu} \left(\frac{2h\nu^3}{c^2} + B_\nu(T)\right). \tag{50}$$

Here, we used $h\nu = h\nu_{u\mathrm{ion}} + \frac{1}{2} m_{\mathrm{e}} v_{\mathrm{e}}^2$, and g_u and g_{ion} are degeneracies of u and ion.

If thermal equilibrium does not hold, (50) should be modified to

$$\sigma_{\mathrm{ion}\to u}(v_{\mathrm{e}}; T) = \frac{g_u h}{2 g_{\mathrm{ion}} m_{\mathrm{e}}^2 v_{\mathrm{e}}^2} \frac{\sigma_{u\to \mathrm{ion}}(\nu)}{\nu} \left(\frac{2h\nu^3}{c^2} + B_\nu(T)\right), \tag{51}$$

so that T should not appear in the equation. As well as the case of bound-bound transitions, the first and second terms can be understood as spontaneous and induced components, respectively. If we neglect the second term, (45) is obtained.

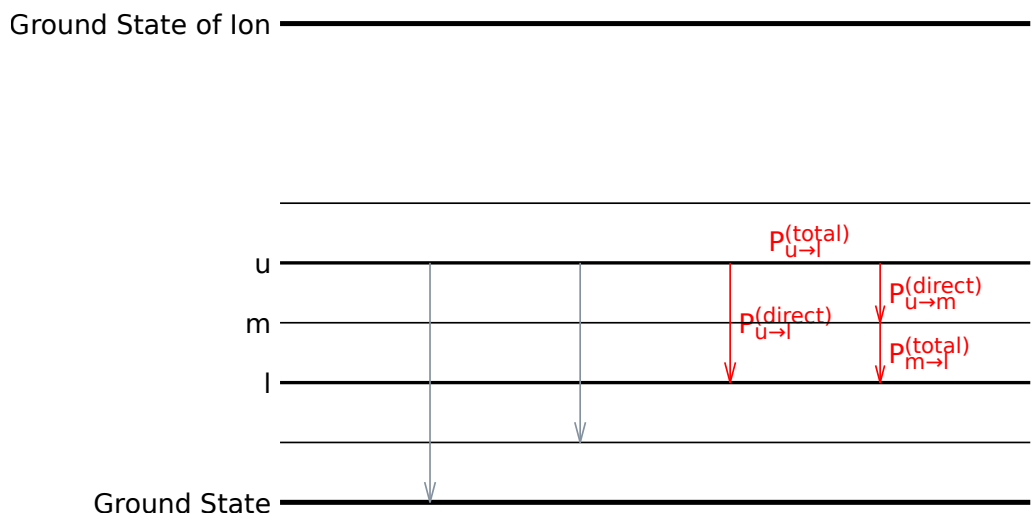

Figure A.5: Explanatory diagram for equation (44). $P^{(\mathrm{total})}_{u\to l}$ is the 'total' recombination rate from the ion to level u. It does not include only the 'direct' transition $P^{(\mathrm{direct})}_{u\to l}$ but also 'direct' transitions to intermediate levels m weighted by the 'total' transition probability $P^{(\mathrm{total})}_{m\to u}$ from these m-s to level l.

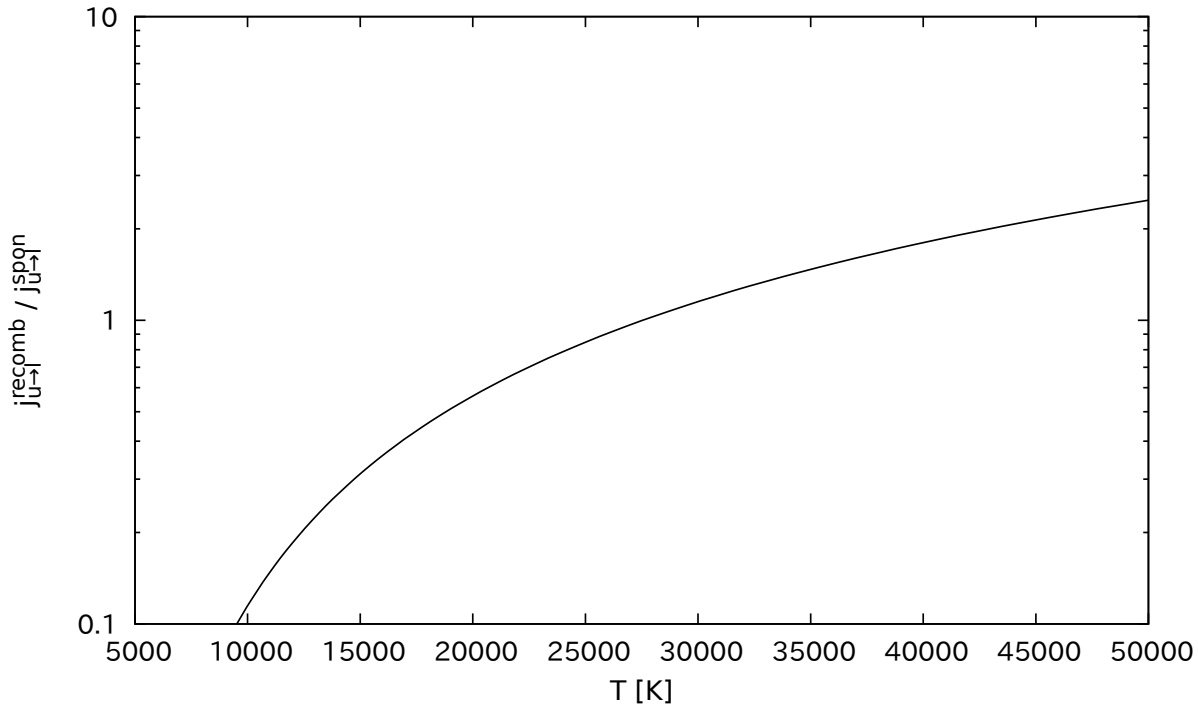

Figure A.6: The ratio of $j^{\mathrm{recomb}}_{u\to l}$ to $j^{\mathrm{spon}}_{u\to l}$ for Hα emission line.

Table A.2: Number of levels for all ions included in our calculation.

Atom	H^-	I	II	III	IV	V	VI	VII	VIII	IX	X	XI	XII	XIII	XIV	XV	XVI
H	1	36	1														
He		237	30	1													
C		242	338	243	64	133	75	1									
N		104	442	306	278	67	109	75	1								
O		199	340	343	324	178	65	141	75	1							
Ne		201	242	188	355	432	234	228	69								
Na		71	35	229	240	380	452	251	214	71							
Mg		152	80	201	264	311	444	476	262	242	74						
Al		257	156	80	201	283	358	463	512	259	234	75					
Si		493	157	147	66	203	279	388									
S		477	324	257	194	216	78										
Ar		203	918	346	382	376	205	174	72								
Ca		184	77	232	378	613	301	514	445	367	79						
Fe		1579	2698	1500	1000	1000	2000	1195	324	712	808	1155	915	826	679	334	77

Table A.3: Bound-bound transitions considered in our calculation.

Line	l	g_l	u	g_u	Oscillator Strength	Einstein's A	λ
Hα	$2s$	2	$3p$	6	0.43488	2.2438×10^{7}	6562.741
	$2p$	6	$3s$	2	1.3590×10^{-2}	6.3102×10^{6}	6562.857
	$2p$	6	$3d$	10	0.69580	6.4618×10^{7}	6562.806
Hβ	$2s$	2	$4p$	6	0.10277	9.6634×10^{6}	4861.290
	$2p$	6	$4s$	2	3.0449×10^{-3}	2.5768×10^{6}	4861.346
	$2p$	6	$4d$	10	0.12180	2.0615×10^{7}	4861.334
He I λ5876	$1s2p\ ^3P$	9	$1s3d\ ^3D$	15	0.61020	7.0699×10^{7}	5875.661
He II	3	18	4	32	0.8421	1.438×10^{8}	4685.70
C III λ5696	$2s3p\ ^1P_1$	3	$2s3d\ ^1D_2$	5	0.34800	4.2905×10^{7}	5695.916
N II λ5679	$2s^22p3s\ ^3P_0$	1	$2s^22p3p\ ^3D_1$	3	0.41120	2.8363×10^{7}	5676.01
	$2s^22p3s\ ^3P_1$	3	$2s^22p3p\ ^3D_1$	3	0.10262	2.1159×10^{7}	5686.213
	$2s^22p3s\ ^3P_2$	5	$2s^22p3p\ ^3D_3$	7	0.34519	5.0957×10^{7}	5679.558
N III λ4640	$2s^23p\ ^2P_{1/2}$	2	$2s^23d\ ^2D_{3/2}$	4	0.38680	6.0037×10^{7}	4634.126
	$2s^23p\ ^2P_{3/2}$	4	$2s^23d\ ^2D_{3/2}$	6	3.8616×10^{-2}	1.1948×10^{7}	4641.851
	$2s^23p\ ^2P_{3/2}$	4	$2s^23d\ ^2D_{5/2}$	6	0.34763	7.1741×10^{7}	4640.644
O I	$2s^22p^3(^4S)3s\ ^5S_2$	5	$2s^22p^3(^4S)3p\ ^5P_1$	3	0.19340	3.5544×10^{7}	7775.388
	$2s^22p^3(^4S)3s\ ^5S_2$	5	$2s^22p^3(^4S)3p\ ^5P_2$	5	0.32240	3.5562×10^{7}	7774.166
	$2s^22p^3(^4S)3s\ ^5S_2$	5	$2s^22p^3(^4S)3p\ ^5P_3$	7	0.45140	3.5586×10^{7}	7771.944
Al II λ6237	$3s4p\ ^3P_0$	1	$3s4d\ ^3D_1$	3	1.0856	6.2230×10^{7}	6226.207
	$3s4p\ ^3P_1$	3	$3s4d\ ^3D_2$	5	0.81420	8.3862×10^{7}	6231.750
	$3s4p\ ^3P_1$	3	$3s4d\ ^3D_1$	3	0.27140	4.6592×10^{7}	6231.633
	$3s4p\ ^3P_2$	5	$3s4d\ ^3D_3$	7	0.91190	1.1140×10^{8}	6243.367
	$3s4p\ ^3P_2$	5	$3s4d\ ^3D_2$	5	0.16284	2.7851×10^{7}	6243.203
	$3s4p\ ^3P_2$	5	$3s4d\ ^3D_1$	3	1.0856×10^{-2}	3.0947×10^{6}	6243.086
Si II $\lambda\lambda$6347/6371	$3s^24s\ ^2S_{1/2}$	2	$3s^24p\ ^2P_{1/2}$	2	0.4140	6.799×10^{7}	6373.133
	$3s^24s\ ^2S_{1/2}$	2	$3s^24p\ ^2P_{3/2}$	4	0.7050	5.833×10^{7}	6348.864

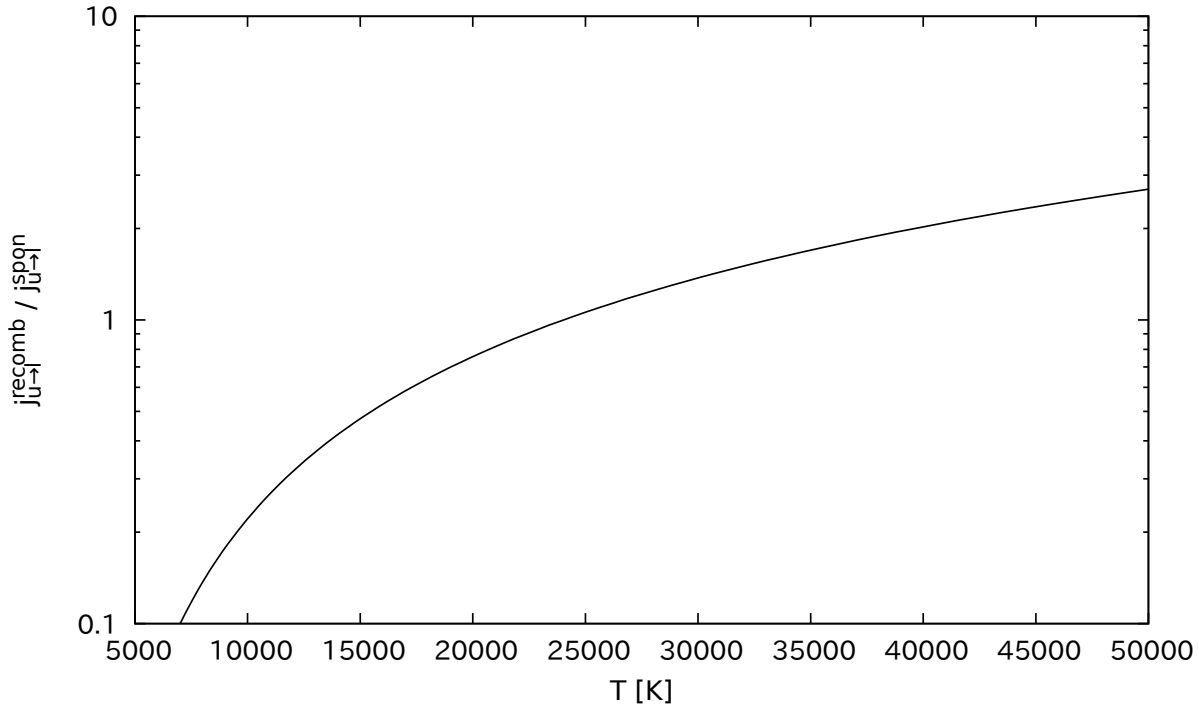

Figure A.7: The same as Figure A.6 but for Hβ.

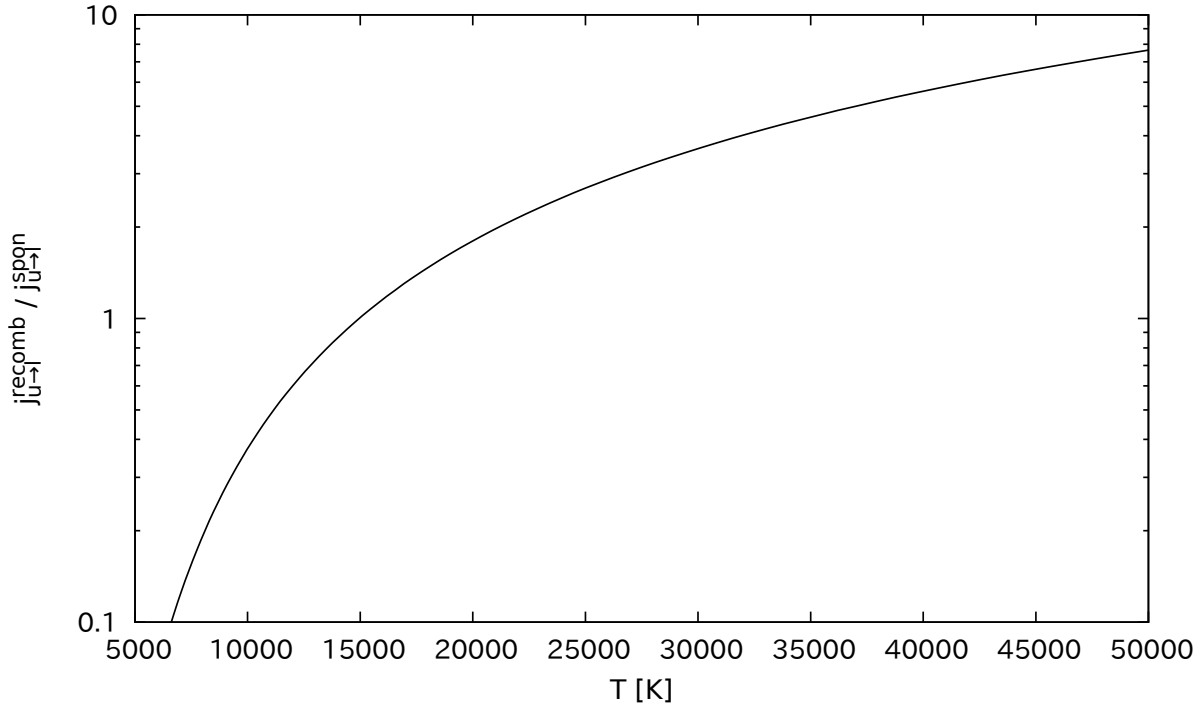

Figure A.8: The same as Figure A.6 but for He I (7065 Å).

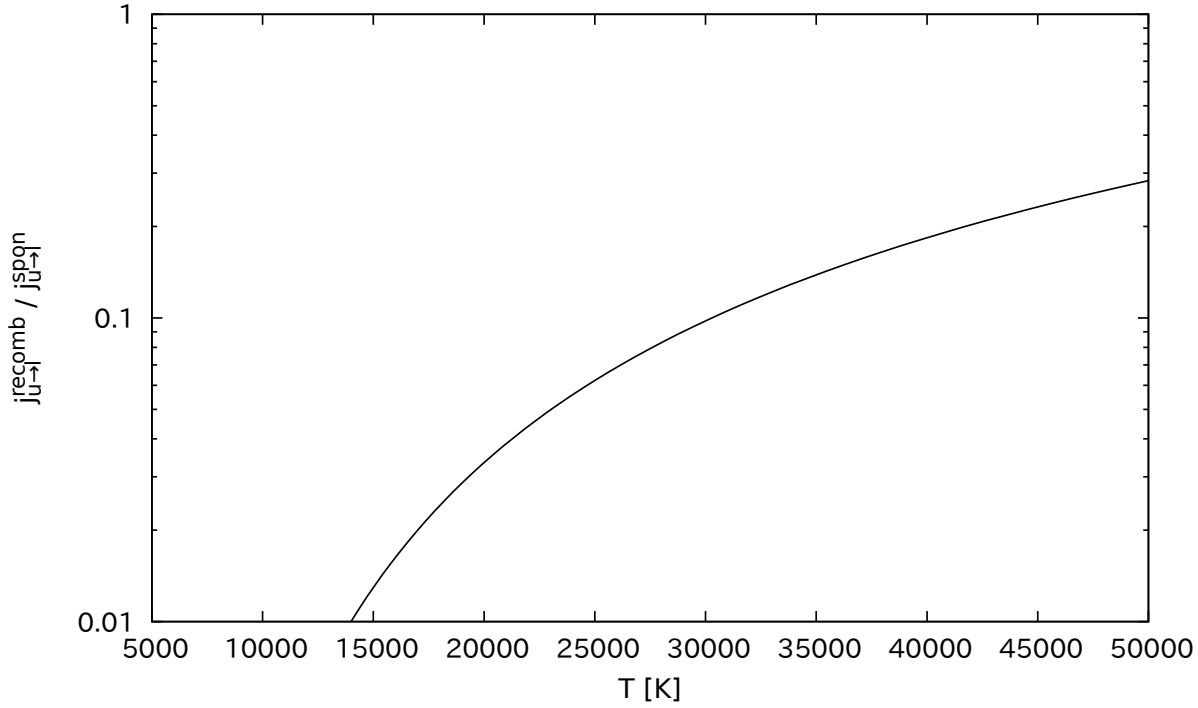

Figure A.9: The same as Figure A.6 but for He II (4686 Å).

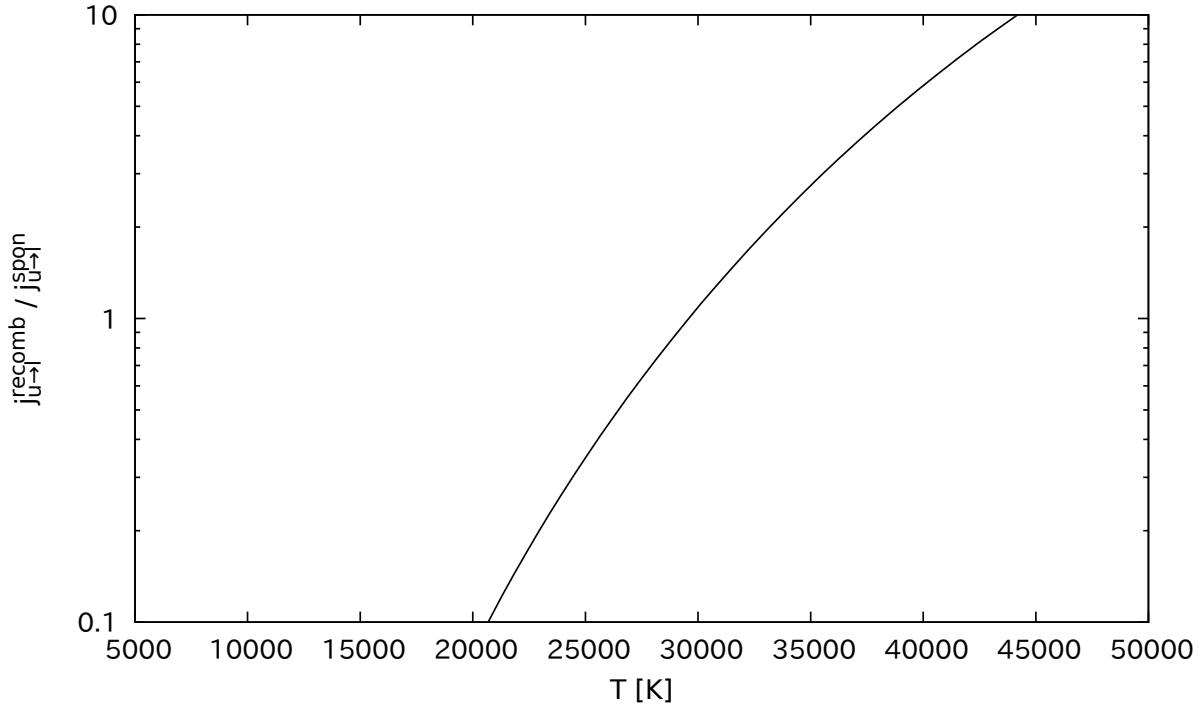

Figure A.10: The same as Figure A.6 but for N II (5679 Å).

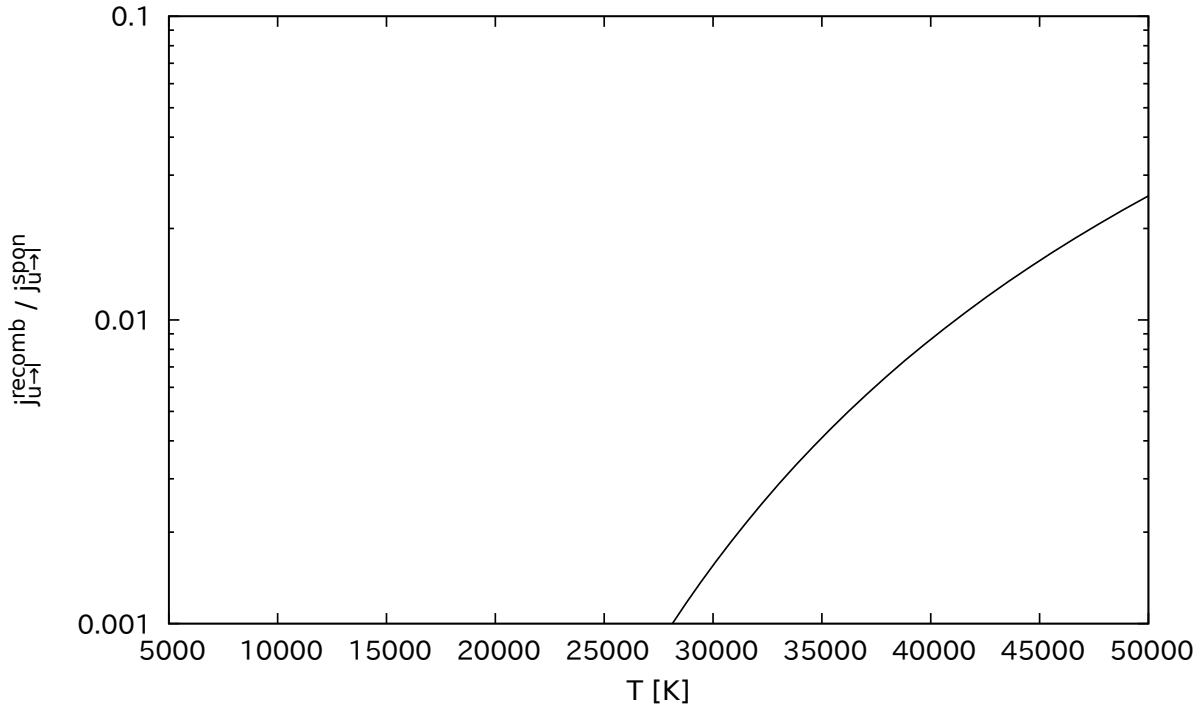

Figure A.11: The same as Figure A.6 but for N III (4640 Å).

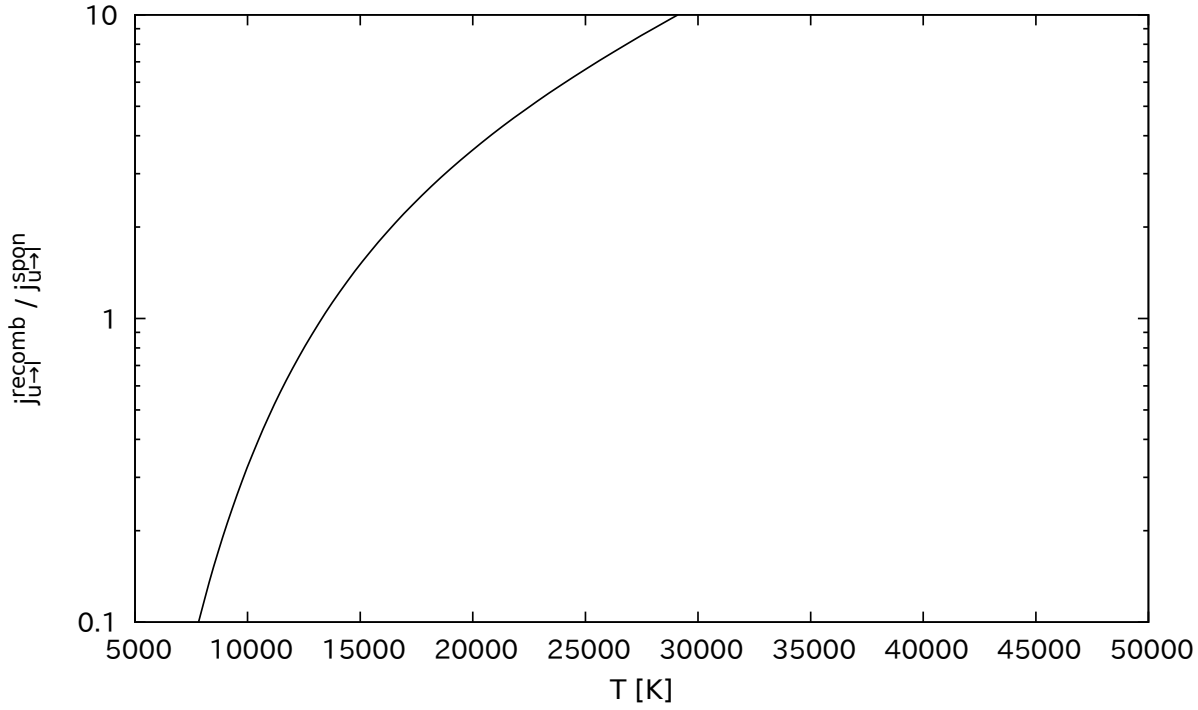

Figure A.12: The same as Figure A.6 but for O I (7773 Å).

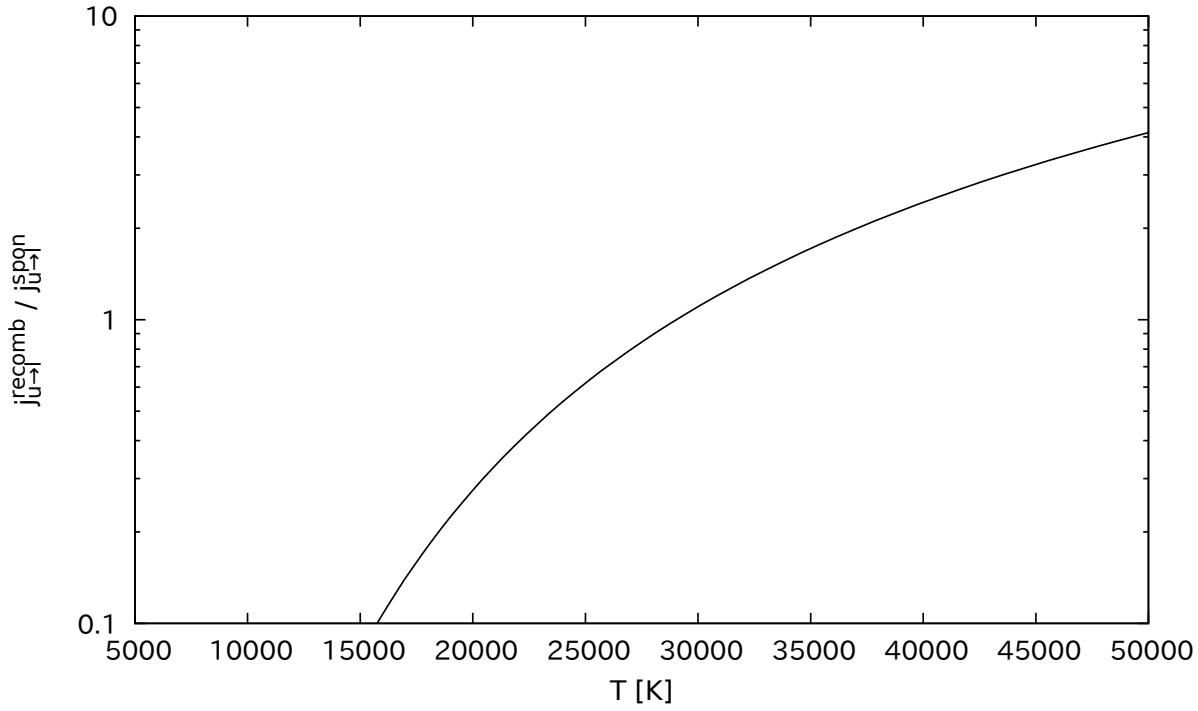

Figure A.13: The same as Figure A.6 but for Al II (6237 Å).

Acknowledgements

In the first place, I would like to thank my supervisor, Keiichi Maeda. At first, he gave me a research theme in theoretical fields. I have learned a lot about the physics of radiation, which is underlying this thesis. Then, considering my suitability, he allowed me to go for observational fields, even though I had achieved almost nothing in that theme, about which I have been feeling sorry. Also, he spent a lot of time giving me many ideas, discussing with me, leading my research, and correcting my English totally bent. It is my pleasure that I have been in his group. I really appreciate the opportunities of discussing with Takashi Nagao, Tatsuya Matsumoto, Roberto Iaconi, Iminhaji Ablimit, Umut Burgaz, Ryo Sawada, Tomoyasu Hayakawa, Ryoma Ouchi, Tomiki Matsuoka, Qiliang Fang, Kohki Uno, Satoko Inutsuka, Mao Ogawa, Masaki Tsurumi, Issei Murata, Yusuke Inoue, and Eleni Koutsiona.

I also would also like to thank the people who belong/belonged to the Okayama Observatory and/or Subaru Telescope Okayama Branch Office, National Astronomical Observatory of Japan, especially Hiroyuki Maehara, Akito Tajitsu, Masaru Kino, Keisuke Isogai, Masaaki Otsuka, and Miho Kawabata, Masayuki Yamanaka, and Kazuya Matsubayashi. I kept making trouble for them, but they kept supporting me. Their efforts, tolerance, and warm atmosphere made me enjoy my research using the Seimei telescope and learn a lot. Of course, I know that a lot of people, including Mikio Kurita, Tetsuya Nagata, Kouji Ohta, and Kazunari Shibata, have worked on the construction of that telescope. I want to thank all of them, though there may be many people whom I do not know because of their graduation, transfer, or retirement.

Next, I would like to thank my collaborators. I especially thank Akira Arai, who not only attracted me to this field through his interesting observation in 2011 but have discussed my research and gave me beneficial comments. Naoto Kojiguchi taught a lot about how to access astronomical open-access data archives. I also appreciate Yusuke Tampo, Jumpei Ito, and Katsuki Muraoka, for a lot of stimulating discussions on their observations which put pressure on me to progress, and their supervisors Daisaku Nogami, who always showed interest in what I am interested in, and Taichi Kato, who always precisely critical to me.

I also thank Keiko Ohara, Miyuki Kawamoto, Yukiko Nakanishi, Noriko Itoh, Takako Nishiyama, Ayako Nagaoka, and Akiko Yamamoto for supporting my graduate school life, and Shota Notsu, Yasuyuki

Wakamatsu, Amanda Cook, Naoto Kurosu, Kento Tokuchi, and Moe Somatsu for the stimulating daily life in the department of Astronomy.

I also appreciate the efforts of variable star and transient observes/hunters, especially Seiji Ueda, Yuji Nakamura, Hideo Nishimura, Tadashi Kojima, Koichi Itagaki, Minoru Yamamoto, Seiichiro Kiyota, Claudio Balcon, Jingyuan Zhao, Filipp Romanov, and Patrik Schmeer, who have longer careers in astronomy than I am, for their cooperation for my research. Also, I appreciate for Masaomi Tanaka, Yuki Mori, Shin Mineshige, Shiu-Hang Lee, Takanori Sasaki. They are not my collaborator in my research, but I remember I felt really happy when they showed interest in my research.

Last but not least, I appreciate my family, Chiyoko Taguchi, Masahiko Taguchi, and Honami Taguchi, who have always supported me and allowed me to do what I want, and my friends who have motivated me, especially Daisuke Taniguchi and Yuri Sakamaki.

Bibliography

Abdo, A. A., Ackermann, M., Ajello, M., et al. 2010, Science, 329, 817, doi: 10.1126/science.1192537

Amari, S., Gao, X., Nittler, L. R., et al. 2001, ApJ, 551, 1065, doi: 10.1086/320235

Andrea, J., Drechsel, H., & Starrfield, S. 1994, A&A, 291, 869

Arai, A., Isogai, M., Yamanaka, M., Akitaya, H., & Uemura, M. 2015, Acta Polytechnica CTU Proceedings, 2, 257

Austin, S. J., Wagner, R. M., Starrfield, S., et al. 1996, AJ, 111, 869, doi: 10.1086/117835

Aydi, E., Chomiuk, L., Izzo, L., et al. 2020, ApJ, 905, 62, doi: 10.3847/1538-4357/abc3bb

Aydi, E., Chomiuk, L., Mikołajewska, J., et al. 2023, MNRAS, 524, 1946, doi: 10.1093/mnras/stad1914

Banerjee, D. P. K., Ashok, N. M., Launila, O., Davis, C. J., & Varricatt, W. P. 2004, ApJL, 610, L29, doi: 10.1086/423171

Barden, S. C., & Armandroff, T. 1995, in Society of Photo-Optical Instrumentation Engineers (SPIE) Conference Series, Vol. 2476, Fiber Optics in Astronomical Applications, ed. S. C. Barden, 56–67

Barden, S. C., Armandroff, T., Muller, G., et al. 1994, in Society of Photo-Optical Instrumentation Engineers (SPIE) Conference Series, Vol. 2198, Instrumentation in Astronomy VIII, ed. D. L. Crawford & E. R. Craine, 87–97

Bellm, E. C., Kulkarni, S. R., Graham, M. J., et al. 2019, PASP, 131, 018002, doi: 10.1088/1538-3873/aaecbe

Bode, M. F., & Evans, A. 2008, Classical Novae, Vol. 43

Boeltzig, A., Bruno, C. G., Cavanna, F., et al. 2016, European Physical Journal A, 52, 75, doi: 10.1140/epja/i2016-16075-4

Boiarchuk, A. A., Galkina, T. S., Gershberg, R. E., et al. 1977, Soviet Ast., 21, 257

Bowesman, C. A., Shuai, M., Yurchenko, S. N., & Tennyson, J. 2021, MNRAS, 508, 3181, doi: 10.1093/mnras/stab2525

Brink, J., Aydi, E., Buckley, D. A. H., et al. 2022, The Astronomer's Telegram, 15270, 1

Chomiuk, L., Metzger, B. D., & Shen, K. J. 2021, ARA&A, 59, 391, doi: 10.1146/annurev-astro-112420-114502

Cox, A. N. 2000, Allen's astrophysical quantities

De, K., Hankins, M. J., Kasliwal, M. M., et al. 2020, PASP, 132, 025001, doi: 10.1088/1538-3873/ab6069

Diehl, R., Dupraz, C., Bennett, K., et al. 1995, A&A, 298, 445

Diehl, R., Halloin, H., Kretschmer, K., et al. 2006, Nature, 439, 45, doi: 10.1038/nature04364

Flewelling, H. A., Magnier, E. A., Chambers, K. C., et al. 2020, ApJS, 251, 7, doi: 10.3847/1538-4365/abb82d

Gaia Collaboration, Prusti, T., de Bruijne, J. H. J., et al. 2016, A&A, 595, A1, doi: 10.1051/0004-6361/201629272

Gaia Collaboration, Vallenari, A., Brown, A. G. A., et al. 2022, arXiv e-prints, arXiv:2208.00211, doi: 10.48550/arXiv.2208.00211

Gandhi, S., & Madhusudhan, N. 2019, MNRAS, 485, 5817, doi: 10.1093/mnras/stz751

Gehrz, R. D., Truran, J. W., Williams, R. E., & Starrfield, S. 1998, PASP, 110, 3, doi: 10.1086/316107

Ginzburg, S., & Quataert, E. 2021, MNRAS, 507, 475, doi: 10.1093/mnras/stab2170

Gray, R. O., & Corbally, Christopher, J. 2009, Stellar Spectral Classification

H. E. S. S. Collaboration, Aharonian, F., Ait Benkhali, F., et al. 2022, Science, 376, 77, doi: 10.1126/science.abn0567

Hachisu, I., & Kato, M. 2001, ApJ, 558, 323, doi: 10.1086/321601

—. 2004, ApJL, 612, L57, doi: 10.1086/424595

—. 2010, ApJ, 709, 680, doi: 10.1088/0004-637X/709/2/680

—. 2015, ApJ, 798, 76, doi: 10.1088/0004-637X/798/2/76

Hachisu, I., Kato, M., Kato, T., & Matsumoto, K. 2000, ApJL, 528, L97, doi: 10.1086/312428

Hack, M., Ladous, C., Jordan, S. D., et al. 1993, Cataclysmic variables and related objects, Vol. 507

Hillier, D. J. 1990, A&A, 231, 116

Hillier, D. J., & Miller, D. L. 1998, ApJ, 496, 407, doi: 10.1086/305350

Hillman, Y., Prialnik, D., Kovetz, A., Shara, M. M., & Neill, J. D. 2014, MNRAS, 437, 1962, doi: 10.1093/mnras/stt2027

Iben, I., J., & Tutukov, A. V. 1985, ApJS, 58, 661, doi: 10.1086/191054

Iijima, T. 2006, A&A, 451, 563, doi: 10.1051/0004-6361:20053984

Iijima, T., Rosino, L., & della Valle, M. 1998, A&A, 338, 1006

Iliadis, C. 2015, Nuclear Physics of Stars, doi: 10.1002/9783527692668

Isogai, K., & Maehara, H. 2020, The Astronomer's Telegram, 13680, 1

Isogai, K., Taguchi, K., Kojiguchi, N., & Tampo, Y. 2020, The Astronomer's Telegram, 14042, 1

Isogai, K., Tampo, Y., Kojiguchi, N., et al. 2021, The Astronomer's Telegram, 14390, 1

José, J., & Hernanz, M. 1998, ApJ, 494, 680, doi: 10.1086/305244

José, J., Hernanz, M., & Iliadis, C. 2006, NuPhA, 777, 550, doi: 10.1016/j.nuclphysa.2005.02.121

José, J., Shore, S. N., & Casanova, J. 2020, A&A, 634, A5, doi: 10.1051/0004-6361/201936893

Kato, M., & Hachisu, I. 1994, ApJ, 437, 802, doi: 10.1086/175041

Kato, M., Hachisu, I., & Saio, H. 2023, MNRAS, 525, L56, doi: 10.1093/mnrasl/slad096

Kato, M., Saio, H., & Hachisu, I. 2017, ApJ, 838, 153, doi: 10.3847/1538-4357/838/2/153

Kato, M., Saio, H., Hachisu, I., & Nomoto, K. 2014, ApJ, 793, 136, doi: 10.1088/0004-637X/793/2/136

Kepler, S. O., Koester, D., & Ourique, G. 2016, Science, 352, 67, doi: 10.1126/science.aad6705

Kippenhahn, R., Weigert, A., & Weiss, A. 2013, Stellar Structure and Evolution, doi: 10.1007/978-3-642-30304-3

König, O., Wilms, J., Arcodia, R., et al. 2022, Nature, 605, 248, doi: 10.1038/s41586-022-04635-y

Kovetz, A., Yaron, O., & Prialnik, D. 2009, MNRAS, 395, 1857, doi: 10.1111/j.1365-2966.2009.14670.x

Kurita, M., Kino, M., Iwamuro, F., et al. 2020, PASJ, 72, 48, doi: 10.1093/pasj/psaa036

Langer, N. 2012, ARA&A, 50, 107, doi: 10.1146/annurev-astro-081811-125534

Lauffer, G. R., Romero, A. D., & Kepler, S. O. 2018, MNRAS, 480, 1547, doi: 10.1093/mnras/sty1925

Lyke, J. E., & Campbell, R. D. 2009, AJ, 138, 1090, doi: 10.1088/0004-6256/138/4/1090

Maeda, K. 2022, in Handbook of X-ray and Gamma-ray Astrophysics, 75

Maeda, K., Taguchi, K., & Fang, Q. 2022, Transient Name Server Classification Report, 2022-3169, 1

Maehara, H., Taguchi, K., Tampo, Y., Kojiguchi, N., & Isogai, K. 2021, The Astronomer's Telegram, 14471, 1

Mahoney, W. A., Ling, J. C., Jacobson, A. S., & Lingenfelter, R. E. 1982, ApJ, 262, 742, doi: 10.1086/160469

Mahoney, W. A., Ling, J. C., Wheaton, W. A., & Jacobson, A. S. 1984, ApJ, 286, 578, doi: 10.1086/162632

Matsubayashi, K., Ohta, K., Iwamuro, F., et al. 2019, PASJ, 71, 102, doi: 10.1093/pasj/psz087

Mikołajewska, J., & Shara, M. M. 2017, ApJ, 847, 99, doi: 10.3847/1538-4357/aa87b6

Miyaji, S., Nomoto, K., Yokoi, K., & Sugimoto, D. 1980, PASJ, 32, 303

Moore, A. M., Kasliwal, M. M., Gelino, C. R., et al. 2016, in Society of Photo-Optical Instrumentation Engineers (SPIE) Conference Series, Vol. 9906, Ground-based and Airborne Telescopes VI, ed. H. J. Hall, R. Gilmozzi, & H. K. Marshall, 99062C

Mowlavi, N., Eggenberger, P., Meynet, G., et al. 2012, A&A, 541, A41, doi: 10.1051/0004-6361/201117749

Munari, U., & Valisa, P. 2021, arXiv e-prints, arXiv:2109.01101. https://arxiv.org/abs/2109.01101

—. 2022, The Astronomer's Telegram, 15796, 1

Munari, U., Valisa, P., & Dallaporta, S. 2021a, The Astronomer's Telegram, 14614, 1

—. 2021b, The Astronomer's Telegram, 14476, 1

Noguchi, K., Aoki, W., Kawanomoto, S., et al. 2002, PASJ, 54, 855, doi: 10.1093/pasj/54.6.855

Nomoto, K. 1984, ApJ, 277, 791, doi: 10.1086/161749

—. 1987, ApJ, 322, 206, doi: 10.1086/165716

O'Brien, T. J., Bode, M. F., Porcas, R. W., et al. 2006, Nature, 442, 279, doi: 10.1038/nature04949

Orio, M., Drake, J. J., Ness, J. U., et al. 2020, ApJ, 895, 80, doi: 10.3847/1538-4357/ab8c4d

Page, K. L., Kuin, N. P. M., Beardmore, A. P., et al. 2020, MNRAS, 499, 4814, doi: 10.1093/mnras/staa3083

Payne-Gaposchkin, C. 1964, The galactic novae

Poggiani, R. 2008, NewA, 13, 557, doi: 10.1016/j.newast.2008.03.001

Politano, M., Starrfield, S., Truran, J. W., Weiss, A., & Sparks, W. M. 1995, ApJ, 448, 807, doi: 10.1086/176009

Prialnik, D. 2009, An Introduction to the Theory of Stellar Structure and Evolution

Quimby, R. M., Shafter, A. W., & Corbett, H. 2021, arXiv e-prints, arXiv:2107.05763. https://arxiv.org/abs/2107.05763

Rafanelli, P., & Rosino, L. 1978, A&AS, 31, 337

Ricker, G. R., Winn, J. N., Vanderspek, R., et al. 2015, Journal of Astronomical Telescopes, Instruments, and Systems, 1, 014003, doi: 10.1117/1.JATIS.1.1.014003

Saizar, P., Pachoulakis, I., Shore, S. N., et al. 1996, MNRAS, 279, 280, doi: 10.1093/mnras/279.1.280

Saizar, P., Starrfield, S., Ferland, G. J., et al. 1992, ApJ, 398, 651, doi: 10.1086/171890

Sako, S., Ohsawa, R., Takahashi, H., et al. 2018, in Society of Photo-Optical Instrumentation Engineers (SPIE) Conference Series, Vol. 10702, Ground-based and Airborne Instrumentation for Astronomy VII, ed. C. J. Evans, L. Simard, & H. Takami, 107020J

Schaefer, B. E. 2021, arXiv e-prints, arXiv:2106.13907. https://arxiv.org/abs/2106.13907

—. 2023, arXiv e-prints, arXiv:2308.13668, doi: 10.48550/arXiv.2308.13668

Schwarz, G. J. 2002, ApJ, 577, 940, doi: 10.1086/342234

Schwarz, G. J., Shore, S. N., Starrfield, S., & Vanlandingham, K. M. 2007, ApJ, 657, 453, doi: 10.1086/510661

Schwarzschild, M., & Härm, R. 1965, ApJ, 142, 855, doi: 10.1086/148358

Shafter, A. W., Taguchi, K., Zhao, J., & Hornoch, K. 2022, Research Notes of the American Astronomical Society, 6, 241, doi: 10.3847/2515-5172/aca2a6

Shappee, B. J., Prieto, J. L., Grupe, D., et al. 2014, ApJ, 788, 48, doi: 10.1088/0004-637X/788/1/48

Shore, S. N., Augusteijn, T., Ederoclite, A., & Uthas, H. 2011, A&A, 533, L8, doi: 10.1051/0004-6361/201117721

Shore, S. N., Teyssier, F., Garde, O., et al. 2021a, The Astronomer's Telegram, 14622, 1

Shore, S. N., Schwarz, G., Bond, H. E., et al. 2003, AJ, 125, 1507, doi: 10.1086/367803

Shore, S. N., Buil, C., Dubovsky, P., et al. 2021b, The Astronomer's Telegram, 14577, 1

Skarka, M., Mašek, M., Brát, L., et al. 2017, Open European Journal on Variable Stars, 185, 1. https://arxiv.org/abs/1709.08851

Starrfield, S., Sparks, W. M., & Shaviv, G. 1988, ApJL, 325, L35, doi: 10.1086/185105

Starrfield, S., Truran, J. W., Sparks, W. M., & Kutter, G. S. 1972, ApJ, 176, 169, doi: 10.1086/151619

Strope, R. J., Schaefer, B. E., & Henden, A. A. 2010, AJ, 140, 34, doi: 10.1088/0004-6256/140/1/34

Taguchi, K. 2022, Transient Name Server Classification Report, 2022-3539, 1

—. 2023a, The Astronomer's Telegram, 15857, 1

—. 2023b, The Astronomer's Telegram, 15911, 1

—. 2023c, Transient Name Server Classification Report, 2023-311, 1

—. 2023d, The Astronomer's Telegram, 16038, 1

—. 2023e, Transient Name Server Classification Report, 2023-1113, 1

—. 2023f, Transient Name Server Classification Report, 2023-2399, 1

—. 2023g, Transient Name Server Classification Report, 2023-2450, 1

Taguchi, K., Fujii, M., & Kato, T. 2023a, The Astronomer's Telegram, 16177, 1

Taguchi, K., & Isogai, K. 2020, The Astronomer's Telegram, 13972, 1

—. 2021a, The Astronomer's Telegram, 14514, 1

—. 2021b, The Astronomer's Telegram, 14576, 1

Taguchi, K., Isogai, K., & Balcon, C. 2021a, The Astronomer's Telegram, 14449, 1

Taguchi, K., Isogai, K., Kawabata, M., & Maehara, H. 2021b, The Astronomer's Telegram, 15035, 1

Taguchi, K., Isogai, K., Kawabata, M., & Yamanaka, M. 2020a, The Astronomer's Telegram, 14258, 1

Taguchi, K., Isogai, K., Kojiguchi, N., & Tampo, Y. 2021c, The Astronomer's Telegram, 14575, 1

Taguchi, K., Isogai, K., Kojiguchi, N., Tampo, Y., & Balcon, C. 2021d, The Astronomer's Telegram, 14370, 1

Taguchi, K., Isogai, K., Shibata, M., et al. 2021e, The Astronomer's Telegram, 14478, 1

Taguchi, K., Ito, J., Balcon, C., & Isogai, K. 2021f, The Astronomer's Telegram, 15043, 1

Taguchi, K., Kawabata, M., Gangopadhyay, A., Singh, A., & Kojiguchi, N. 2023b, Transient Name Server Classification Report, 2023-1232, 1

Taguchi, K., Kawabata, M., Isogai, K., et al. 2021g, The Astronomer's Telegram, 15039, 1

Taguchi, K., Kawabata, M., Zhao, J., & Gao, X. 2023c, The Astronomer's Telegram, 16304, 1

Taguchi, K., Kojiguchi, N., & Isogai, K. 2020b, The Astronomer's Telegram, 14204, 1

Taguchi, K., Kojiguchi, N., Tampo, Y., et al. 2020c, The Astronomer's Telegram, 13947, 1

Taguchi, K., & Maeda, K. 2023, Transient Name Server Classification Report, 2023-2385, 1

Taguchi, K., & Maehara, H. 2020, The Astronomer's Telegram, 13519, 1

—. 2021, The Astronomer's Telegram, 14962, 1

Taguchi, K., Maehara, H., Fujii, M., & Kato, T. 2021h, The Astronomer's Telegram, 14699, 1

Taguchi, K., Maehara, H., Isogai, K., Tampo, Y., & Ito, J. 2021i, The Astronomer's Telegram, 14858, 1

Taguchi, K., Maehara, H., Isogai, K., et al. 2021j, The Astronomer's Telegram, 14472, 1

Taguchi, K., Namekata, K., Okamoto, S., et al. 2020d, The Astronomer's Telegram, 13975, 1

Taguchi, K., & Otsuka, M. 2022, Transient Name Server Classification Report, 2022-3298, 1

Taguchi, K., Qiliang, F., & Kawabata, M. 2023d, Transient Name Server Classification Report, 2023-117, 1

Taguchi, K., Shibata, M., Masayuki, Y., et al. 2021k, The Astronomer's Telegram, 15072, 1

Taguchi, K., Tampo, Y., Isogai, K., et al. 2020e, The Astronomer's Telegram, 14266, 1

Taguchi, K., Ueta, T., & Isogai, K. 2021l, The Astronomer's Telegram, 14838, 1

Taguchi, K., Uno, K., Kawabata, M., et al. 2021m, The Astronomer's Telegram, 14374, 1

Taguchi, K., Uno, K., & Tsurumi, M. 2023e, Transient Name Server Classification Report, 2023-2569, 1

Taguchi, K., Yamamoto, M., Moriyama, M., et al. 2022a, The Astronomer's Telegram, 15623, 1

Taguchi, K., & Yamanaka, M. 2022, Transient Name Server Classification Report, 2022-432, 1

Taguchi, K., Yamanaka, M., & Isogai, K. 2022b, The Astronomer's Telegram, 15420, 1

Taguchi, K., Yamanaka, M., Isogai, K., & Balcon, C. 2021n, The Astronomer's Telegram, 14412, 1

Taguchi, K., Maeda, K., Maehara, H., et al. 2023f, ApJ, 958, 156, doi: 10.3847/1538-4357/ad0133

Tajitsu, A., Aoki, W., Kawanomoto, S., & Narita, N. 2010, Publications of the National Astronomical Observatory of Japan, 13, 1

Tajitsu, A., Sadakane, K., Naito, H., Arai, A., & Aoki, W. 2015, Nature, 518, 381, doi: 10.1038/nature14161

Takeda, L., Diaz, M., Campbell, R., & Lyke, J. 2018, MNRAS, 473, 355, doi: 10.1093/mnras/stx2285

Tanaka, J., Nogami, D., Fujii, M., et al. 2011, PASJ, 63, 911, doi: 10.1093/pasj/63.4.911

Tang, S., Cao, Y., & Kasliwal, M. M. 2013, The Astronomer's Telegram, 5607, 1

Vanlandingham, K. M., Starrfield, S., & Shore, S. N. 1997, MNRAS, 290, 87, doi: 10.1093/mnras/290.1.87

Vanlandingham, K. M., Starrfield, S., Shore, S. N., & Sonneborn, G. 1999, MNRAS, 308, 577, doi: 10.1046/j.1365-8711.1999.02731.x

Vasini, A., Matteucci, F., Spitoni, E., & Siegert, T. 2023, MNRAS, 523, 1153, doi: 10.1093/mnras/stad1440

White, N. E., Giommi, P., Heise, J., Angelini, L., & Fantasia, S. 1995, ApJL, 445, L125, doi: 10.1086/187905

Whitney, B. A., & Clayton, G. C. 1989, AJ, 98, 297, doi: 10.1086/115146

Williams, R. 2012, AJ, 144, 98, doi: 10.1088/0004-6256/144/4/98

Williams, R. E. 1992, AJ, 104, 725, doi: 10.1086/116268

Williams, R. E., Phillips, M. M., & Hamuy, M. 1994, ApJS, 90, 297, doi: 10.1086/191864

Woodward, C. E., Greenhouse, M. A., Gehrz, R. D., et al. 1995, ApJ, 438, 921, doi: 10.1086/175134

Yamanaka, M., Uemura, M., Kawabata, K. S., et al. 2010, PASJ, 62, L37, doi: 10.1093/pasj/62.5.L37

Yaron, O., Prialnik, D., Shara, M. M., & Kovetz, A. 2005, ApJ, 623, 398, doi: 10.1086/428435